



Improving Multi-Scatter Reconstruction Algorithms for Background Rn222 Decays Inside the LUX-ZEP LXe Detector

Submitted by

Daniel John Radford

Thesis Advisor

Dr. Jim Dobson

Department of Physics and Astronomy

A thesis submitted to University College London in partial fulfilment of the
requirement for the degree of Masters of Physics

2021

Abstract

Department of Physics and Astronomy

Masters of Physics

Improving Multi-Scatter Reconstruction Algorithms for Background Rn222 Decays Inside the LUX-ZEP LXe Detector

by Daniel John Radford

LUX-ZEPLIN (LZ) is a state of the art next generation detector with the goal of observing a direct scatter of a WIMP particle. LZ is 50 times more sensitive than previous generation detectors. The experiment utilises a seven ton active volume of liquid xenon, surrounded by a two phase time projection chamber (TPC). The TPC records primary (S1) and secondary (S2) scintillation signals produced by scatter events, enabling their localisation and energy deposits to be recorded. This thesis presents an account of the evidence which has provoked wide acceptance throughout the physics community that dark matter must exist and justifies the particle search effort. The research in this thesis focuses on problematic radioactive backgrounds in the detector such as ^{222}Rn and ^{220}Rn . The energy deposits due to the decays of these backgrounds are analysed, and a method is provided to identify them using the pulse information collected via the photo-multiplier tubes (PMTs). It was found that mono-energetic lines can be isolated for ^{212}Pb decays to the excited state ^{212}Bi [238], which may enable the tagging of these events in-situ. This could lead to improvements in the measurement of problematic backgrounds of Rn and the measurements of flow patterns within the fiducial volume.

Acknowledgements

I would like to deeply thank the following people, without whom I would not have been able complete this thesis, or in fact, make it to the end of my Masters program at all. Dr. Jim Dobson, for his time, endless patience and encouragement while guiding me through my thesis. My parents, whom without I would not have made it half as far as I have. Your belief in me, however unjustified, has been an immensely motivating factor in my studies. Your emotional and financial support has made all of this possible. Finally, my close friends, who have provided one too many distractions along the way.

Contents

Abstract	i
Acknowledgements	ii
1 Introduction	1
1.1 What's the Matter?	1
1.1.1 Initial Evidence from the Coma Cluster	2
1.1.2 Theoretical Evidence from Computer Simulations	3
1.1.3 Rotation Curves	4
1.1.4 Gravitational Lensing	5
1.1.5 Evidence from Cosmic Microwave Background	7
1.1.6 Particle Candidates	9
1.2 Detection Methods	10
1.2.1 Overview of Detector Types	10
1.2.2 Nobel Gas TPC's	11
1.2.3 Direct WIMP Scattering	14
1.2.4 Signal Generation	16
1.2.5 Signal Energy Scales	18
1.3 Background Mitigation	20
1.3.1 General Mitigation Strategies	20
1.3.2 Background Mitigation Review of LUX	22
2 Analysis	26
2.0.1 Aim of Project	26
2.1 Monte Carlo Truth Study of $^{214}/^{212}\text{Pb}$ Decays	26
2.1.1 Background	26
2.1.2 Feasibility to Tag Excited States	28
2.2 Analysis of Reconstructed Quantities	32
2.2.1 LZ Event Viewer	32
2.2.2 Pulse Classification Performance	34
2.2.3 Event Selection	37
2.2.4 Tagging Decays from Reconstructed Data	38
2.3 Conclusion	41
Bibliography	43

List of Figures

- | | | |
|-----|--|----|
| 1.1 | Example of a simulated evolution of a galaxy structure with an initial non-zero velocity dispersion. As time progresses it can be seen the structure evolves from a stable disk to an axisymmetric bar and eventually to an unstable pressure supported disk. Figure acquired from [9]. | 3 |
| 1.2 | This figure demonstrates the stabilising effect of adding a static halo on galaxy simulations. As the ratio of halo to disk mass approaches 2, the kinetic energy to gravitational potential energy approaches the critical stability value of 0.14. Stability is reflected in the linearity of the curve over time. Figure acquired from [10]. | 4 |
| 1.3 | Figure depicts the expected rotation curve from the distribution of luminiferous mass. The observed rotation curve is significantly large This implies that a large proportion of the mass in the M33 is unseen. Figure acquired from [13]. | 5 |
| 1.4 | The plot demonstrates the idealized Keplerian decline $\frac{1}{\sqrt{r}}$ of rotational velocity compared to the measured velocity for NGC3198. Figure acquired from [14]. | 6 |
| 1.5 | Mass and light distribution map of the 1E0657-558 cluster merger. The green contours show the mass distribution while the heat map shows the light distribution. High collision of gaseous particles results in x-ray emission which can be seen in the glowing yellow regions. However, the majority of the mass density has moved past this region. Figure acquired from [16]. | 7 |
| 1.6 | The temperature power spectrum of the CMB for Ω_{CMD} ranging between 0.11-0.43 is shown in varying hues of blue. The black line is the measured power spectrum taken from Plank 2018 results [17]. Figured acquired from [18]. | 8 |
| 1.7 | A graph showing the self-shielding of external gamma rays and neutrons in xenon. The red and blue lines show a clear exponential reduction in scatter events as distance increases from the lateral edge of the TPC chamber wall. At $\approx 2cm$ and $\approx 6cm$ a tenfold decrease in scattering events is achieved. Figure acquired from [30]. | 12 |
| 1.8 | Predicted recoil spectra for $100GeV/c^2$ WIMP scattering in different Nobel gas medium. The assumed dark matter halo parameters are given in the legend. Figure acquired from [31]. | 13 |
| 1.9 | For a WIMP of mass m_x , the nuclear recoil spectra are given for various common ultra-sensitive low background target materials. At high energies the rate for heavier target nuclei (larger A^2) is suppressed. At lower energies the rate is larger for large A^2 . Figured acquired from [18]. | 15 |

1.10 Cartoon illustration of a dual phase time projection chamber. Photomultiplier tubes are arranged around the chamber and represented as cylinders. E1 and E3 denote the drift field and extraction field respectively. The legend gives an example of the expected pulse sizes of the S1 and S2 signals generated by a nuclear recoil event. It can be seen that the S2 signal is broader due to number of ionization electrons inducing the signal. Figure acquired from [31].	17
1.11 Schematic diagram of xenon ionization , excitation and recombination events which generate S1/S2 signals in the 1Z PMTs. Figure acquired from [37].	18
1.12 A γ radioactivity spectrum of the low-background photo-multiplier tubes used in the LXe time projection chamber. Figure acquired from [18].	21
1.13 Graphical illustration of Radon and Thoron decay chains down to their stable isotopes. Figure acquire from [43].	22
1.14 Nuclear recoils have a greater recombination fraction r than ER. This higher fraction allows for discrimination between the two using the S1/S2 signal. The two distinctive ER and NR bands can be seen on the right. The lowest fraction of the NR band is using in the WIMP search to avoid leakage from the ER band. Figure acquired from [37].	23
1.15 Comparison of simulated γ -ray spectrum modelled from LUXSim (red dotted) and the measured γ -ray spectrum (black) in the Lux fiducial volume. Energy deposits were reconstructed using S1/S2 signals, both single scatter and multi-scatter events were included. At higher energies there is a much large systematic uncertainty visible from the horizontal error bars. Figure acquired from [44].	24
1.16 Data generated for Radon daughters from the LUX 85.3 day WIMP search run. The quoted energies relate to the Q-value for each decay which can be compared with the measured energies form the run for a sense of accuracy. Figure acquired from [44].	25
2.1 The legend denotes the colour code for each excited Bi state. The Q-value of 1019 KeV can clearly be seen on the x-axis. The total amount of decays to each excited state correctly represents the appropriate intensities given in table 2.1. This indicates the truth data is accurately modeling ^{214}Pb decays and that algorithm is identifying them correctly.	27
2.2 Results for ^{214}Pb decays. The x-axis shows the bins of the normalised absolute separation between the mean energy weighted positions of Bi associated energy deposits and β associated energy deposits.	29
2.3 Results for ^{214}Pb decays. The x-axis shows the bins of the x-y projected separation between the mean energy weighted positions of Bi associated energy deposits and β associated energy deposits.	29
2.4 Results for ^{214}Pb decays. The x-axis shows the bins of the z projected separation between the mean energy weighted positions of Bi associated energy deposits and β associated energy deposits.	29
2.5	29

2.6	The legend denotes the colour code for each excited Bi state. The Q-value of 569.1 is can clearly be seen on the x-axis. The % of total decays to each excited state correctly represents the intensities give in table 2.2. This indicates the truth data is accurately modeling ^{212}Pb decays and the algorithm is identifying them correctly.	30
2.7	Results for ^{212}Pb decays. The x-axis shows the bins of the normalised absolute separation distance between the Bi cluster and the β cluster.	31
2.8	Results for ^{212}Pb decays. The x-axis shows the bins of the x-y projected normalised absolute separation distance between the Bi cluster and the β cluster.	31
2.9	Results for ^{212}Pb decays. The x-axis shows the bins of the z projected normalised absolute separation distance between the Bi cluster and the β cluster.	31
2.10	31
2.11	Example of the full LZAp event display. The S1 pulse is highlighted green, the S2 is highlighted blue.	33
2.12	Highlighted S1 pulse from figure 2.11.	33
2.13	Highlighted S2 pulse from figure 2.11 The width of the pulse is in agreement with the predict width from the cluster separation analysis	33
2.14	Example of a multi-scatter S2	33
2.15	33
2.16	Scatter plot for Pf50ns vs $\text{Log}_{10}[\text{area}]$	34
2.17	Scatter plot for top bottom asymmetry (TBA) vs $\text{Log}_{10}[\text{area}]$	35
2.18	Scatter plot of pulse width vs $\text{Log}_{10}[\text{area}]$. A fraction of S2 pulses are being misclassified as SE pulses	36
2.19	Scatter plot of pulse width vs $\text{Log}_{10}[\text{area}]$. A cut has been applied to remove the misclassified S2s	36
2.20	Scatter plot of the first S2 pulse area vs the second S2 pulse area for all events in the data set.	38
2.21	Histogram of the second S2 pulse area vs first S2 pulse area. The heatmap indicates the intensity of events at given areas.	39
2.22	Histogram of the second S2 pulse area vs first S2 pulse area, with correction factors applied.	40
2.23	Second S2 pulse bottom area VS S1 area.	41

List of Tables

2.1	Branched decay data for ^{214}Pb . β^- -decay intensity: 100%. Q=1019 KeV. Daughter ^{214}Bi products are shown in the final column. The final entry shows the naked β -decay to the ground state.	28
2.2	Branched decay data for ^{212}Pb . β^- -decay intensity: 100%. Q=569.1 KeV. Daughter ^{212}Bi products are shown in the final column. The final entry shows the naked β -decay to the ground state.	30
2.3	Performance of the event classification algorithm with maximum area threshold cuts applied for 142809 events. Pile up consists of events with multiple S1 and S2 pulses. No pulse consists of events with no S1 or S2 pulses. Multi-scatter consists of events with one S1 and more than one S2.	37
2.4	The matrix shows the percentage groupings of S1 and S2 events.	37

1

Introduction

1.1 What's the Matter?

Modern developments in cosmology have shown that a significant fraction of the energy density of observable Universe is composed of non-baryonic matter. Recent calculations suggest the non-baryonic content Ω_D is as much as $\approx 26.8\%$. This percentage is five times larger than the contribution of baryonic matter Ω_M ($\approx 4.9\%$) which constitutes all the 'ordinary' matter we see around us (protons, neutrons and electrons etc). The matter density of the Universe can be determined using predictions from big bang nucleosynthesis and cosmic microwave background (CMB) analysis. This is a testament to the precision of measurements made in modern cosmology, which can reveal the fine detailed structure of the Universe. The governing equation for the total energy density of the Universe follows from the Friedman equation, derived from the Robertson-Walker Einstein field equations for a homogeneous, isotropic expanding Universe. The space-time line element for this metric is given below:

$$ds^2 = -c^2 + a(t)^2 [dr^2 + S_k(r)^2 d\Omega^2] \quad (1.1)$$

The Hubble parameter can be expressed as a Taylor expansion of the expansion rate at some time t and the expansion rate today:

$$a(t) = a_0 [1 + \frac{\dot{a}_0}{a_0} (t - t_0) + \frac{\ddot{a}_0}{a_0} \frac{(t - t_0)^2}{2!}] \quad (1.2)$$

Where the Hubble parameter is:

$$H = \frac{\dot{a}}{a} \quad (1.3)$$

The Einstein field equations in terms of the Hubble parameter are:

$$H^2 = \frac{8\pi\rho}{3} + \frac{\Lambda}{3} - \frac{k}{3} \quad (1.4)$$

Which can be rewritten as:

$$1 = \frac{8\pi\rho}{3H^2} + \frac{\Lambda}{3H^2} - \frac{k}{a^2 H^2} \quad (1.5)$$

The above defines the dimensionless density parameters:

$$\Omega = \frac{8\pi\rho}{3H^2} = \frac{\rho}{\rho_{crit}} \quad (1.6)$$

And

$$\Omega_\Lambda = \frac{\Lambda}{3H^2} \quad (1.7)$$

Therefore, the total energy density can be expressed as:

$$\Omega_{total} - 1 = \frac{k}{a^2 H^2} \quad (1.8)$$

where the k term denotes the total curvature of the Universe. Ω_{total} can be expressed in terms of the matter contribution Ω_B, Ω_D (baryonic/non-baryonic) and radiation Ω_r

The Plank Collaboration (2015) CMB survey confirmed these measurements. It was also found that 68.3% of the energy density is composed of dark energy $\Omega\Lambda$. In total, 95% of the Universe's energy content is accounted for by a 'dark' component. Non-baryonic matters existence (more often referred to as 'dark matter') is now widely supported by physicists, although there are other theories which have received notable support (i.e. Modified Newtonian Dynamics). The amount of scientific support dark matter has received is not a reflection on the state of knowledge available on dark matters nature or properties. Experiments have been undertaken and many more are still currently being developed to test a variety of hypothetical dark matter particle candidates. But, as of yet, a dark matter particle has never been directly or indirectly detected.

1.1.1 Initial Evidence from the Coma Cluster

The search for a direct detection of dark matter has eluded particle physicists and cosmologists alike since Zwicky first utilised the virial theorem to postulate its existence in 1933. The virial theorem was originally developed by Clausius for evaluating the mean kinetic energies of spatially constraint fluids in thermodynamics [1]. Zwicky's astronomical application of the theorem infamously demonstrated that the amount of luminiferous matter content contained within Coma cluster of galaxies should result in the cluster dissipating [2]. The expected dissipation is a result of the measured recessional velocities of individual galaxies within the cluster exceeding the escape velocity determined by the gravitational force provided by the observable luminiferous matter within cluster.

The discrepancy between the observed stability of the cluster and the measured recessional velocities can be resolved by postulating the existence of a type of yet unknown and undetected non-luminiferous matter called dark matter, which provides the necessary additional gravitational support to stabilise the cluster. The required mass to gravitationally bind the cluster is approximately $10^{14} M_\odot$ solar masses, but assuming a mass to light ratio of unity, only $10^{12} M_\odot$ solar masses are observed. Using the currently accepted value of the Hubble constant $H_0 = 67.270.66 km/s/Mpc$ the mass to light ratio required to stabilise the cluster is ≈ 60 [3, 4].

Intracluster free hydrogen gas was originally put forward as an early suggestion as to what the non-luminiferous matter could be. This suggestion was later shown to be theoretically impossible. To ensure the outward kinetic pressure of the gas overcomes its self-gravitation, a temperature exceeding $10^8 Kelvin$ is required. However, x-ray emission data limited the possible temperature of any intracluster gas to lie between $10^4 - 10^6 Kelvin$ [5]. Further x-ray emission analysis demonstrated that a hot

intracluster gas could only account for 2% of the unseen non-luminiferous matter [6]. The discrepancy observed in the Coma Cluster was the first indication of the presence of dark matter. Computing simulations attempting to emulate stable galaxy structures have provided more weight to the dark matter hypothesis.

1.1.2 Theoretical Evidence from Computer Simulations

Technological breakthroughs in computing during the 20th century, such as vast improvements in rapid access memory (RAM), enabled simulations of the interactions between many body objects such as clusters and galaxies to be performed. This was possible since an increase in RAM increases the total number of calculations per second a computer is able to perform. These simulations provide a method to probe stability and structure formation of stellar objects, providing critical theoretical insight into how non-luminiferous matter may be distributed [7, 8].

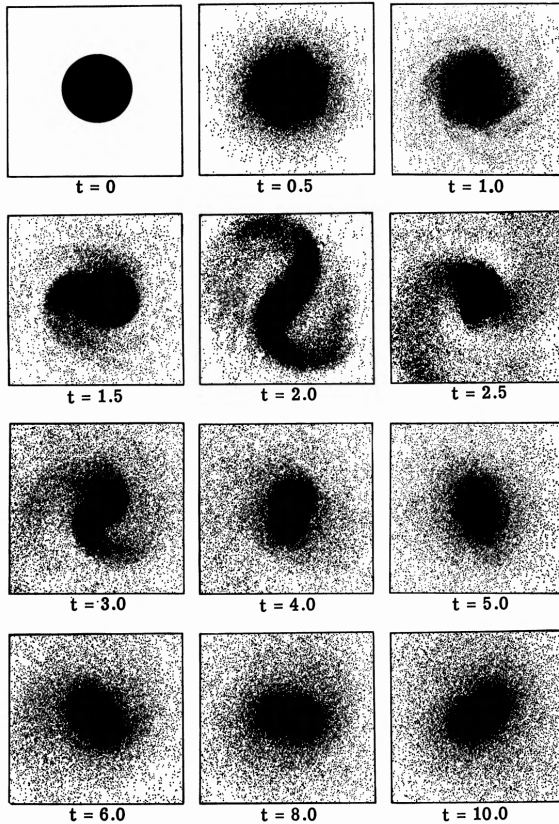


FIGURE 1.1: Example of a simulated evolution of a galaxy structure with an initial non-zero velocity dispersion. As time progresses it can be seen the structure evolves from a stable disk to an axisymmetric bar and eventually to an unstable pressure supported disk. Figure acquired from [9].

A key insight was developed by Ostriker and Peebles, building on previous work by Hohl. Hohl demonstrated that an initialised cold stable disk would rapidly develop asymmetric instabilities and form unstable pressure supported disks and therefore should not form long lasting structures in the Universe. Where cold indicates

that the random individual motion of stars is negligible in comparison to the disk (hot would indicate the random motion of individual stars is not negligible). Since cold rotationally supported disks are observed in abundance in the Universe and Hohl's simulations suggest they should not be observed, clearly other factors need to be considered. Ostriker and Peebles proposed that if the ratio between the rotational kinetic energy and gravitational potential energy was 0.14 ± 0.02 , a limit of stability is found [10]. To reduce the kinetic/potential ratio to the value of critical stability, a static spherical dark halo of mass was inserted into the structure of the galaxy. Since the massive dark halo was static, the extra mass would not contribute to the rotational energy, but it would increase the gravitational potential of the galaxy. A dark halo to disk mass ratio of ≈ 2 provides the necessary stabilising ratio of 0.14.

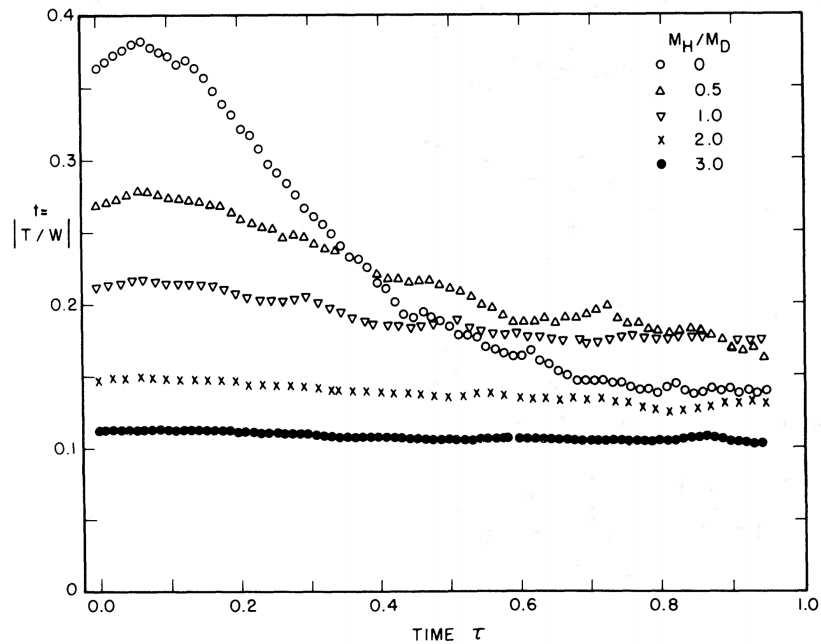


FIGURE 1.2: This figure demonstrates the stabilising effect of adding a static halo on galaxy simulations. As the ratio of halo to disk mass approaches 2, the kinetic energy to gravitational potential energy approaches the critical stability value of 0.14. Stability is reflected in the linearity of the curve over time. Figure acquired from [10].

A critical observation from Ostriker and Peebles is that for stability to be achieved, the majority of the mass in the galaxy is contained within the static stabilising dark halo. Toomre provided a physical interpretation of how the dark halo provides the stabilising effect. He proposed that the massive dark halo reduces the length scales of unstable matter which propagate through the disk, therefore reducing their effect on the overall stability [8].

1.1.3 Rotation Curves

Hyperfine transitions in neutral hydrogen lead to a discrete spectral emission at 21 cm [11]. Radio-waves in this frequency band are also transparent to interstellar dust.

Coupled with the fact that hydrogen is the most abundant element in the Universe makes these emissions crucial to astronomy. Since the wavelength of the transition is known, the velocities (and rotational velocities) of faraway objects can be measured using the Doppler Effect. Rotation curves relate the rotational velocity of a galaxy to the distance towards the center. The rotational velocity depends on the inward gravitational attraction and the outward centrifugal forces. Therefore, from rotation curves the mass distribution of a galaxy can be inferred. From Newton's law of gravitational the velocity is expected to fall off with a Keplerian decline $v(r) \sim \frac{1}{\sqrt{r}}$ (see figure 1.4). Rotation curves can be compared with the light distribution collected using a technique called surface photometry. Comparing these two distributions of a galaxy can reveal un-luminiferous mass because the amount of light emitted can also be related to the mass distribution. For galaxy M33, the results exhibited a large discrepancy between the mass required to gravitationally bind the galaxy due to its rotational velocity and the mass inferred from the photometry data, indicating that a significant amount of un-luminiferous mass should contained within the galaxy and that dark halos are real [12].

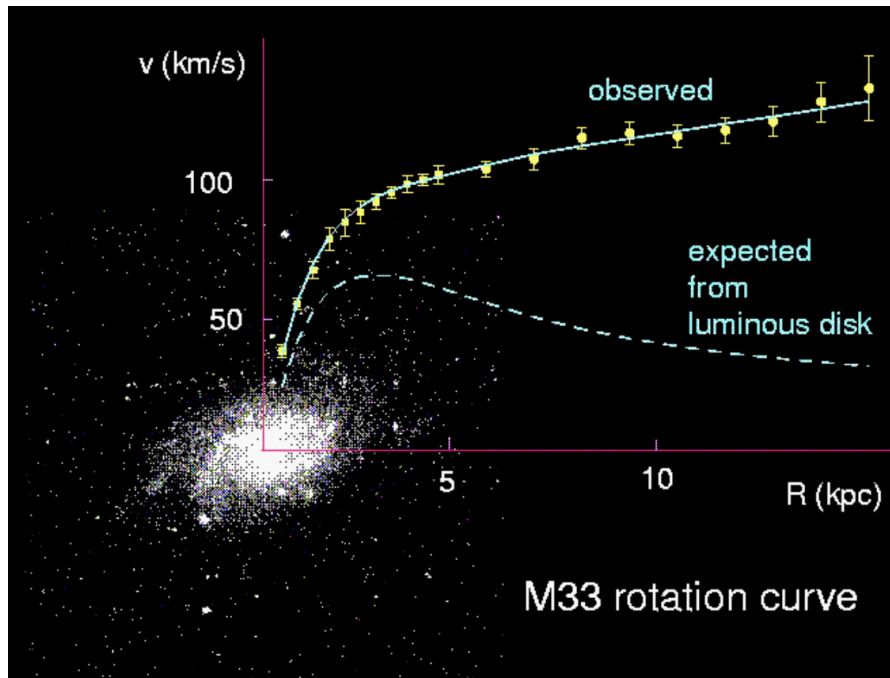


FIGURE 1.3: Figure depicts the expected rotation curve from the distribution of luminiferous mass. The observed rotation curve is significantly large This implies that a large proportion of the mass in the M33 is un-seen. Figure acquired from [13].

1.1.4 Gravitational Lensing

Einstein's general theory of relativity introduces a phenomenon known as gravitational lensing. Gravitational lensing occurs when a massive object causes the surrounding space-time to curve. Light propagating through curved space-time follows a curved

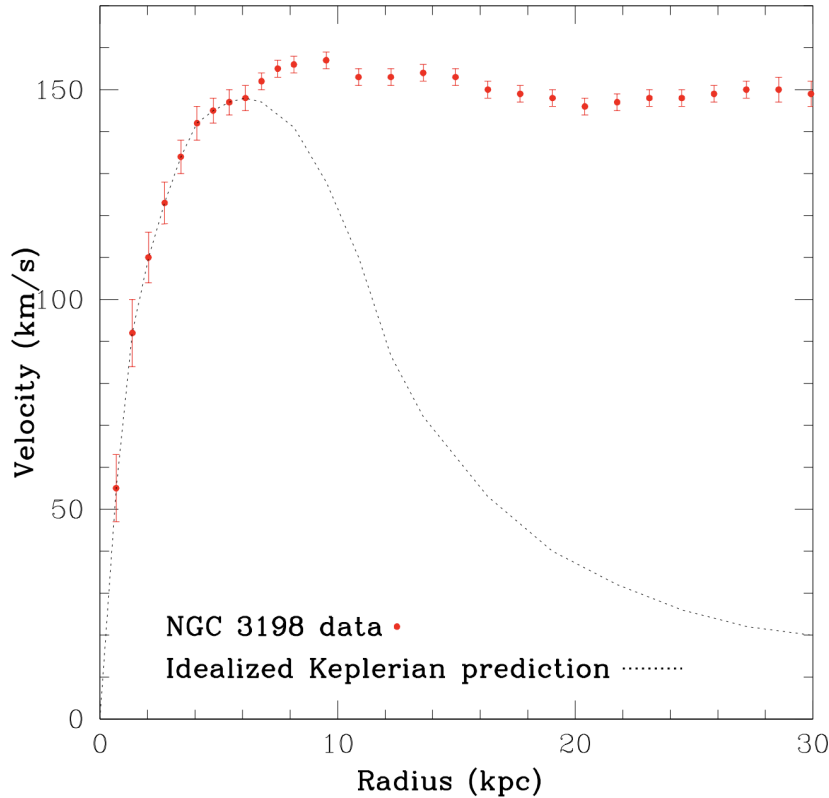


FIGURE 1.4: The plot demonstrates the idealized Keplerian decline $\frac{1}{\sqrt{r}}$ of rotational velocity compared to the measured velocity for NGC3198. Figure acquired from [14].

trajectory from an external frame of reference. This is because in general relativity light travels through space-time in null geodesics. This is analogous to how aeroplanes travel in ‘straight lines’ around the curved surface of the globe. Therefore, massive stellar objects such as clusters of galaxies can act as a lens for light emitted from objects behind them. This effect can cause galaxies to look stretched or distorted. Strong gravitational lensing can cause multiple images of the same object to appear around a central mass. A visually spectacular example of this effect is the formation of Einstein rings.

Methods have been developed which enable the mass distribution of the massive object causing the space-time warping to be reconstructed [15]. These methods were used on the 1E0657-558 cluster merger (now known as the Bullet Cluster). Mass distribution maps exposed that the luminiferous mass distribution did not fit the gravitational potential distribution. An 8σ offset was found between the baryonic mass and the total mass of the cluster [16]. As the clusters collided, the gaseous components separated from the larger structures (galaxies/stars). The gravitational potential maps revealed that the non-baryonic also separated from the gaseous components. This is expected as dark matter is weakly interacting.

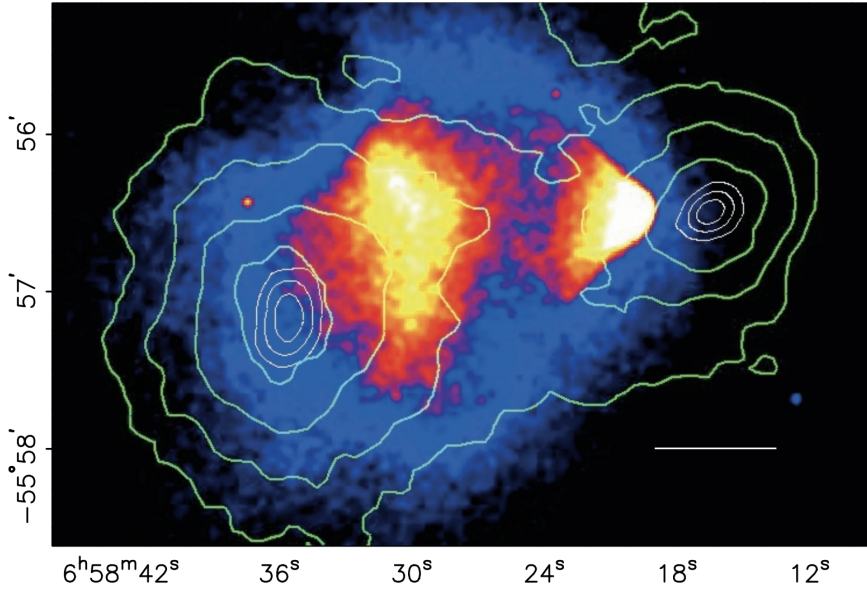


FIGURE 1.5: Mass and light distribution map of the 1E0657-558 cluster merger. The green contours show the mass distribution while the heat map shows the light distribution. High collision of gaseous particles results in x-ray emission which can be seen in the glowing yellow regions. However, the majority of the mass density has moved past this region.

Figure acquired from [16].

1.1.5 Evidence from Cosmic Microwave Background

On the largest scale the Universe has been found to be flat, smooth and homogeneous. The Universe also has a black-body spectrum temperature of $\approx 2.7\text{K}$ caused by isotropic photons emitted from the Big Bang. As the Universe expanded and cooled from its initial dense state to $z \approx 1000$, photons and electrons eventually decoupled, resulting in a source of the relic photons. It is these photons which form the cosmic microwave background (CMB). Analysing patterns in the CMB reveals detailed information about the composition and history of the Universe. Relic photons originating from regions of high matter density show up as 'cold regions' in the CMB, whereas regions of low matter density show up as 'hot regions'. The actual variation in temperature between hot and cold regions is frozen at $\approx 10^{-5}\text{ Kelvin}$. Analysing the temperature variation gives a picture of matters homogeneity throughout the Universe, however, analysing baryon acoustic oscillations provides information on dark matters contribution to Ω_M

Baryonic and non-baryonic matter coalesced in the early Universe due to gravity and density fluctuations in the distribution of the matter. The regions of coalesced matter exerted a restoring outward pressure against the inward gravitational attraction. Similar adiabatic behaviour can be observed in harmonic oscillators. Oscillatory behaviour occurs due to a cycle of outward pressure dominating the inward attractive force; and vice versa. This happens because the time scale for gravitational collapse t_g (which is proportional to the speed of causality c) is competing with the time scale for

outward pressure to build t_p . The limiting factor for pressure to build is the speed of sound. This relationship is captured by the Jeans length equation:

$$\lambda_j = 2\pi c_s t_g \quad (1.9)$$

During the epoch of decoupling between baryons and photons the speed of sound was massively decreased, causing the Jeans length to become much shorter. This caused the acoustic oscillations to cease, resulting in massive gravitational collapse and enabling large scale structure formation to occur. The acoustic oscillations at the time of decoupling can still be observed in the CMB power spectrum as temperature differentials and their analysis reveals precise information on the energy density Ω_M of the Universe (See section:1.10). This possible because non-baryonic matter does not interact under the influence of the electromagnetic interaction. This is essential because the outward pressure experienced by baryonic matter under gravitational collapse is caused by radiation. Therefore, non-baryonic matter does not experience the outward pressure and only contributes to the collapse phase of the cycle. The outcome of this effect is that the rate of formation of large scale structures is massively increased due to the presence of dark matter. Variations in temperature in the CMB provide a measurement of the amount of dark matter present at the epoch of baryonic-photon decoupling because without dark matter, the variations in temperature would be much smaller than are actually measured.

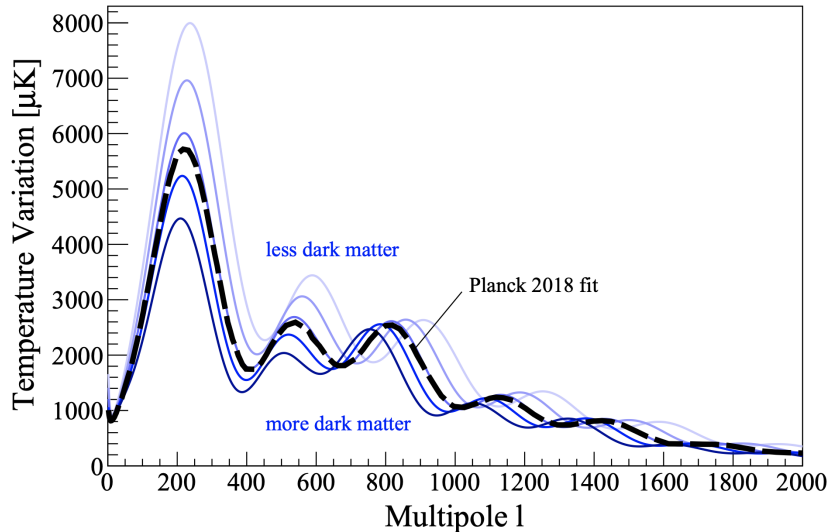


FIGURE 1.6: The temperature power spectrum of the CMB for Ω_{CMD} ranging between 0.11-0.43 is shown in varying hues of blue. The black line is the measured power spectrum taken from Plank 2018 results [17].

Figured acquired from [18].

1.1.6 Particle Candidates

General relativity and astronomical observational evidence have shown the Universe to be expanding. In the early Universe different categories of particles freeze out and decouple at particular red-shifts z , becoming relic particles. Cosmological relics are formed when thermal equilibrium between interacting particles can no longer be maintained. For particles to remain in equilibrium they must remain within thermal contact. This is defined by one interaction in a period set by the Hubble time. The expansion of space causes the interaction rate to fall resulting in the particle freezing out. Once a type of particle has frozen out the co-moving number density becomes fixed [13].

$$\Omega_{\chi h^2} \approx \frac{3 \cdot 10^{-27}}{\langle \sigma_A v \rangle} \text{cm}^3 \text{s}^{-1} \quad (1.10)$$

The first order energy density contribution of a particle χ (defined in 1.10) is determined by the annihilation cross section and temperature. Weakly interacting massive particles (WIMPs) are loosely defined as massive particles with an interaction strength comparable to the weak interaction and a Ω_M contribution of approximately unity. The freeze out temperature for WIMPs is roughly 4-5% of the particles mass. This results in WIMPs having non-relativistic velocities upon decoupling, which is commonly referred to as cold dark matter.

A variety of different particles have been considered to be candidates for dark matter. The neutrino, which decoupled with photons when the average kinetic energy between them was $\approx 2\text{MeV}$, is no longer considered likely. This is due to the upper limit of the neutrino rest mass being $\approx 1.1\text{eV}$. The significant deviation between the rest mass and decoupling energy results in relic neutrinos being highly relativistic. This is referred to as hot dark matter. Hot dark matter has been shown to result in a top down structure formation. This is where large astronomical systems such as galaxy clusters form first, which later disperse into smaller structures [19]. Computer models of a top down approach have predicted that galaxies would form at a red-shift of 2. Astronomical observations have shown that galaxies have red-shifts much larger than 2, suggesting galaxies formed earlier in the Universe. For neutrinos to form the majority of the mass found in dark matter halos, their rest mass must exceed 30 eV [20]. The upper limit of neutrino rest mass is given to be 1.1 eV. This experimental contradiction results in the neutrino hot dark matter model being very unlikely to be correct.

However, the cold dark matter model results in a bottom up approach to structure formation. Non-relativistic relic particles ensure that the density fluctuations in the non-baryonic fluid present in the early Universe can expand instead of propagating. Consequently, small scale structures form first (i.e. galaxies) which is congruent with measurements of red-shifts [21].

Axions were presented as a solution to the strong C-P problem (charge-parity) [22]. Charge-parity symmetry arises from the notion that if a particle is swapped with its partner anti-particle (i.e. electron/positron) the laws of physics should remain invariant, apart from an inversion in the spatial coordinates. This effect can be observed by placing an electron/positron in a constant electric field. The amplitude of acceleration will for both particles will be the same (because electrons and positrons have the same mass), but the trajectory will be in the opposite direction (because of opposite charge).

Modern particle physics has shown that charge conjugation and parity is not a perfect symmetry. C-P violations are observed in higher order weak interactions in the neutral K meson system [13]. One hypothesis for the asymmetry between matter and anti-matter in the Universe is the breaking of this symmetry. Quantum Chromodynamics (QCD) describes the strong interaction as underlying gauge theory. It predicts that non-perturbative effects in the strong interaction should result in large charge-parity violations. Neutral particles such as the neutron limit such large violations due to their lack of a dipole. A solution to this problem put forward by Peccei and Quinn was to introduce a global U(1) symmetry which can be voluntarily broken. The axion is the boson of the broken U(1) symmetry. The axion could be a potential candidate for a cold dark matter (CDM) model because of constraints found via laboratory experiments and astronomical observations such as supernova. If axions exist, they must couple weakly to matter and could not have been in thermal equilibrium in the early Universe, making axions a non-relativistic relic. The predicted mass of axions is between 10^{-2} and 10^{-4} eV, which means extremely sensitive experiments are required to detect the particle [23, 24, 25]. Since the mass of axions is expected to be so small, for them to make up the matter content of dark halos their energy density contribution Ω_χ must be huge.

The neutralino χ is another primary possibility for a dark matter particle candidate. Neutralinos are the lightest super-symmetric particle predicted by the modern Minimal Supersymmetric Standard Model (MSSM). The neutralino consists of a mix of the photino, zino and higgsino particles, which are supersymmetric partners of the photon, Z boson and Higgs boson respectively. The neutralino is thought to be charge neutral and stable under super-symmetry theory if R-parity is conserved. If it turns out that R-parity is not a conserved symmetry, the neutralino would not exist for a sufficient amount of time to constitute a viable dark matter candidate. If neutralino exist, they are predicted to have been produced in abundance in the early Universe, weakly interacting with radiation and matter. Again, as the temperature of the Universe decreased due to expansion, the interaction rate of neutralinos drops (resulting in a decreasing number density) below the Hubble expansion rate. This results in relic neutralinos forming which have been predicted to contribute significantly to the total energy density of the Universe Ω . The gauge coupling properties and hypothetical mass of the neutralino suggest a total energy contribution of $\Omega_M \approx 3$. Many researchers in the dark matter research community believe the neutralino to be a likely dark matter candidate, however there are many other super-symmetric particle candidates which arise from MSSM which are not mentioned here.

1.2 Detection Methods

1.2.1 Overview of Detector Types

There exists a variety of dark matter detector designs. These include anorganic crystals, cryogenics, bubble chambers and Nобal gas dual phase time projection chambers (TPCs). Each design has a specific detection mechanism and as such inherits certain advantages and pitfalls.

Anorganic Crystal Detectors were first implemented for WIMP detection by Ahlen et al. [26]. The detector utilised a 0.72kg mass of high purity Germanium crystals

(HPGe) which are sensitive to induced charge signals from a dark matter particle. The crystal acts as a semiconductor and is highly sensitive to low energy events. A dark matter particle with a low amount of energy is able to create an electron-hole pair which results in numerous signal carriers. Due to the creation of a high amount of signal carriers these types of detectors have a high energy resolution. HPGe detectors have issues when scaling for mass due to high levels of electronic noise caused by the high capacitance of Ge diodes. Current state of the art anorganic crystal detectors use arrays of NaI(Tl) instead to increase the target mass. The downside to using NaI crystals is the high intrinsic background [27]. Since scintillating crystals are searching for the annually modulating signal of WIMPs having a low intrinsic background is a highly desirable trait and more effective detection methods have been developed since.

Cryogenic Crystalline Detectors measure the heat signal generated by phonons emitted from a WIMP interaction. To measure the heat signal, the detector must be placed within cryogenic conditions ($\leq 50mK$), minimizing its heat capacity. This can be seen directly via the detectors sensitivity equation below:

$$\sigma^2 = c_1 kT(TC + c_2 E) \quad (1.11)$$

The above equation shows how the sensitivity of the detectors depends upon the energy deposit E , the operation temperature T , the temperature dependent heat capacity C and the specific thermal coupling constants c_1, c_2 . The coupling constants are $\approx \mathcal{O}(1)$ and are related to the read out noise and heat bath parameters. Germanium crystals are also well suited for cryogenic detectors, but silicon is also commonly used. Cryogenic detectors provide high precision and resolution for energy measurements. Modern state of the art detectors can reach down to $\leq 5\text{GeV}/c^2$ mass WIMPs [28].

Bubble chambers utilise super-heated refrigerants ($\text{CF}_3\text{I}, \text{C}_3\text{F}_8, \text{C}_4\text{F}_{10}$ etc...) as target masses. The super-heated liquids are suspended just below boiling point such that an energy deposit via a WIMP interaction will induce a micro-volume phase transition into the gas phase and produce a bubble. The likelihood of bubble formation is dependent on the stopping power $\frac{dE}{dx}$ of the recoiling molecule. It is possible to refine the experimental parameters such that only nuclear recoil events will lead to bubble formation. This includes nuclear recoils caused by neutrons and α -particles, as well as WIMPs [29]. It is possible to reduce electronic recoils caused by γ and β radiation by up to a factor of $< 10^{-9}$. This effectively removes all dominant ER backgrounds from the detector. α -particle induced recoils can also be identified and rejected due to the specific acoustics of when the bubble dissipates. A notable downside with bubble chambers is the downtime after an energy deposit event. After a bubble is formed, it must be removed via compression. To reset the chamber, it must be decompressed to return the liquid refrigerant back to its original state. Bubble chambers however do have the benefit of being able to operate with a variety of target refrigerants (previously listed) which allows them to search a broad section of the WIMP parameter space.

1.2.2 Nobel Gas TPC's

Nobel liquid detectors (such as LUX-ZEP) utilise scintillation and ionization properties of a variety of Nobel gases. A key benefit of this category of detector is the ability to detect single interaction events, detectors utilising Anorganic Crystals (AC) designs

cannot. Nobel gases such as xenon have the property of a reduced background of long lived radioactive isotopes. This is a huge benefit as these isotopes produce scintillation events which undesirably mimic WIMP interactions.

A second important property of xenon in particular is the large size of its nucleus. A large nucleus increases the likelihood of a scatter event since the spin-independent cross section scales with the atomic number squared, a^2 . Considering the weak nature of the interaction of any suspected dark matter particle, increasing the probability of an interaction is highly desirable. Argon gas would be a possible alternative and has the added benefit of a much lower material cost. However, Argon obtained from atmospheric sources contains the radioactive isotope ^{39}Ar with a specific activity of 1Bq/Kg which would considerably add to the background of the detector, therefore reducing its sensitivity.

Current liquid xenon time projection chambers have a sensitivity to signals as small as a single photon or electron. This makes them particularly suited for rare event searches. Liquid xenon also has a density of $\approx 3\text{g/cm}^3$ which gives xenon self-shielding properties from external radiation. This occurs because the tightly packed dense structures mean the majority of extrinsic radiation will interact with the outer layer of xenon inside of the chamber. The radiation and background material will therefore cluster at the outer edges of the central TPC, falling off with an exponential distribution with respect to distance towards the central volume. Although this voids part of the detector volume, it creates an inner 'fiducial volume' which benefits from the extra shielding [30]. The fiducial volume at LZ holds 5.6 tonnes of liquid xenon.

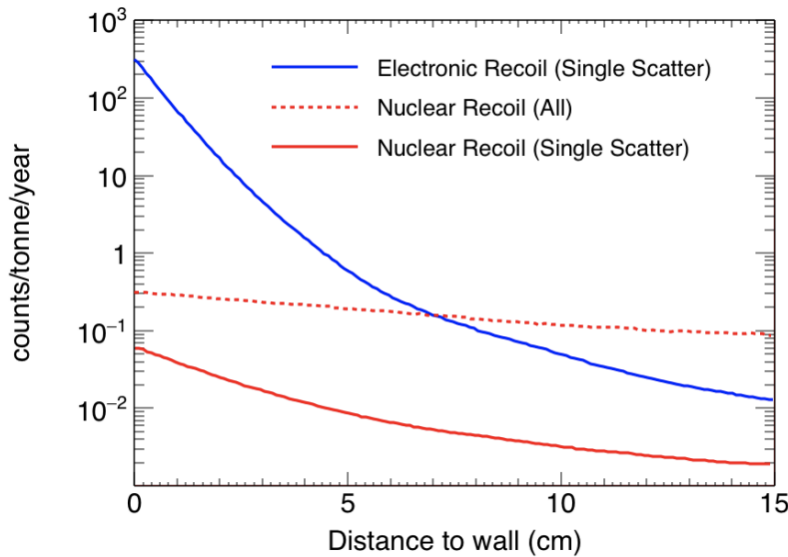


FIGURE 1.7: A graph showing the self-shielding of external gamma rays and neutrons in xenon. The red and blue lines show a clear exponential reduction in scatter events as distance increases from the lateral edge of the TPC chamber wall. At $\approx 2\text{cm}$ and $\approx 6\text{cm}$ a tenfold decrease in scattering events is achieved. Figure acquired from [30].

The fundamental detection mechanism for Nobel gas detectors is that a dark matter

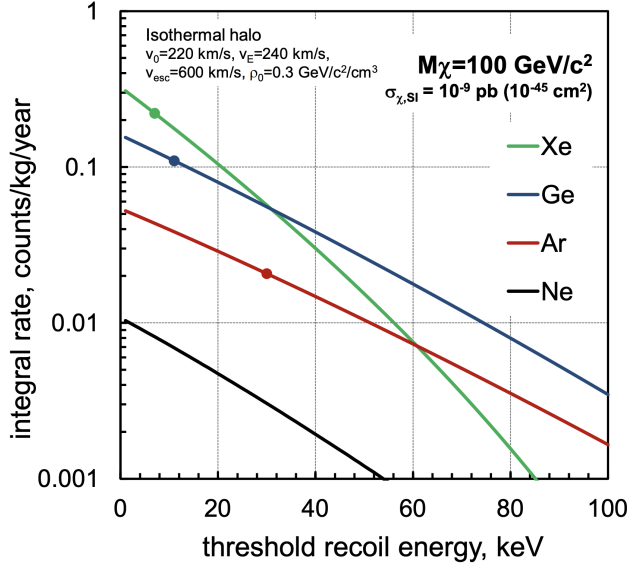


FIGURE 1.8: Predicted recoil spectra for $100\text{GeV}/c^2$ WIMP scattering in different Nobel gas medium. The assumed dark matter halo parameters are given in the legend. Figure acquired from [31].

particle could elastically scatter off a xenon nuclei, inducing a nuclear recoil which deposits kinetic energy into the detector which can then be measured. The recoil energy spectrum of WIMPs is expected to be below $\approx 100\text{KeV}$ and thus detectors are required to have extremely low energy thresholds. The expected energy range of the deposit of $1 - 100\text{KeV}$ means the initial recoil velocity of the nucleus is of the same order as the atomic electrons. This means the scattered xenon atom retains the majority of its electrons while translating through the liquid. As the recoiling xenon is translating through a medium of its own type, each subsequent scatter can transfer a large proportion of its initial recoil energy. This results in a multiplicity of ancillary recoils which produce scatters of comparable energy to the primary event [31]. As the atom recoils through the medium, it will exchange electrons with neighbouring atoms. However, since the majority of electrons are retained, the struck xenon will move through the medium with either a low effective charge or possibly as a neutral atom.

An array of photo-multiplier tubes (PMTs) at either end of the detector amplify detected electrons by several orders of magnitude ($10^5 - 10^7$) via the photoelectric effect. The top array can resolve the location of the nuclear recoil site in the x-y plane via geometrical light acceptance. The depth of the recoil (z-coordinate) can be determined by the difference in time Δt between the primary (S1) and secondary signal (S2). This is possible because the time for the photons from the primary event to hit the PMT is negligible, whereas the drift electrons which produce the secondary scintillation signal have a constant saturated drift velocity through the medium.

1.2.3 Direct WIMP Scattering

Astrophysical observations from the Bullet Cluster, large scale structure formation and the collisions of galaxies have revealed information about the possible nature of a dark matter particle [16]. However, low background scattering experiments such as LUX, collisions at the large hadron collider (LHC) and measurements of dark matter annihilation decay products from the sun, hope to provide a direct measurement method to probe the physical properties of the hypothetical particle [32]. These properties include its interaction cross section, coupling and mass.

WIMPs are charge neutral, therefore the most likely interaction with barionic matter is an elastic scatter off the nuclei of a target atom. The likelihood of a scatter event off an electron is minuscule in comparison. In the event of a WIMP-nuclei scatter, momentum will be transferred which results in a nuclear recoil (NR). For a target nucleus mass m_N the expected rate of scattering is:

$$\frac{dR}{dE_{nr}} = \frac{\rho_0 M}{M_n m_x} \int_{v_{min}}^{v_{esc}} v f(v) \frac{d\sigma}{dE_{nr}} dv \quad (1.12)$$

E_{nr} denotes the energy of the induced nuclear recoil. The scattering cross section is denoted σ . The WIMP mass is denoted m_x . The active target mass of the detector is denoted M . The local dark matter density is given as $\rho_0 = 0.3 \text{ GeV}/c^2/\text{cm}^3$. The function $f(v)$ describes the incoming velocity distribution of WIMPs towards the detector in the detectors frame of reference. WIMPs with a velocity above $v_{esc} = 544 \text{ km s}^{-1}$ will escape the gravitational potential caused by the Milky Way [33]. For a given target nucleus, the minimum velocity for an incoming WIMP to induce a nuclear recoil is:

$$v_{min} = \sqrt{\frac{E_{nr} m_n}{2} \cdot \frac{(m_n + m_x)^2}{(m_N m_x)^2}} = \sqrt{\frac{E_{nr} m_N}{2} \frac{1}{u^2}} \quad (1.13)$$

For a detector run time of T the total number of observed events is:

$$N = T \int_{E_{low}}^{E_{high}} dE_{nr} \epsilon(E_{nr}) \frac{dR}{E_{nr}} \quad (1.14)$$

The detector efficiency is denoted ϵ . The maximum recoil energy E_{high} and the minimum E_{low} . This equation is derived from integrating equation 1.13 in terms of energy.

As the energy tends towards E_{low} (see figure 1.9), equation 1.12 is best described by the decreasing exponential function:

$$\frac{dR}{dE_{nr}} \propto \exp\left(-\frac{E_{nr}}{E_0} \frac{4m_x m_N}{(m_x + m_N)^2}\right) \quad (1.15)$$

WIMPs coherently interact with all nucleons of the target nucleus. This is a result of the large de Broglie wavelength $\lambda = h/q$ in small momentum transfers. Since the interaction mechanism for dark matter and baryonic matter is unknown, the governing interaction equation must include spin-dependent and spin-independent interactions. The scattering cross section for a WIMP-nucleus interaction is;

$$\frac{d\sigma}{dE_{nr}} = \frac{m_N}{2v^2 u^2} (\sigma_{SI} F_{SI}^2(E_{nr}) + \sigma_{SD} F_{SD}^2(E_{nr})) \quad (1.16)$$

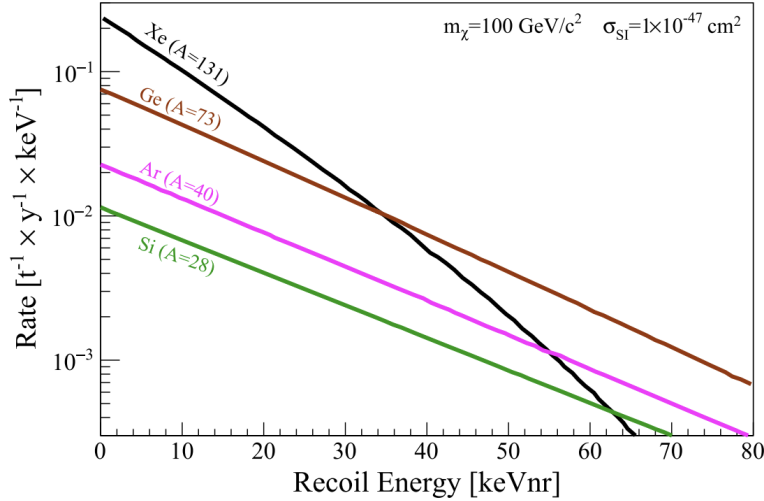


FIGURE 1.9: For a WIMP of mass m_χ , the nuclear recoil spectra are given for various common ultra-sensitive low background target materials. At high energies the rate for heavier target nuclei (larger A^2) is suppressed. At lower energies the rate is larger for large A^2 . Figure acquired from [18].

F_{SI} and F_{SD} denote the spin independent and spin-dependent form factors respectively. σ_{SI} and σ_{SD} denote the spin-independent and spin-dependent cross section respectively. The spin-independent interaction can be described by either a scalar ($\mathcal{L}_s \sim \bar{\chi}\chi\bar{q}q$) and vector ($\mathcal{L}_s \sim \bar{\chi}\gamma^u\chi\bar{q}\gamma^u q$) bi-linear co-variant, or a linear combination of the two. The spin-dependent bi-linear co-variant is described by an axial vector ($\mathcal{L}_s \sim \bar{\chi}\gamma^u\gamma_5\chi\bar{q}\gamma^u\gamma_5 q$). Full details of this calculation can be found here [34].

Large momentum scatters are associated with WIMPs with a smaller de Broglie wavelength and as such only a subsection of the nucleus is involved in the interaction. The loss of coherence is accounted for in the spin dependent and independent form factors F_{SI} and F_{SD} . These form factors are more relevant for larger target nuclei such as Xenon (i.e - at LUX). The spin-independent cross section is proportional to the mass number of the target nuclei $\sigma_{SI} \propto A^2$. Therefore, heavier nuclei such as Xenon will experience a higher scatter rate and is consequently a prime target for use in direct detection experiments. Experimental constraints give a maximal value for the cross section between WIMPs and nucleons as $\sigma_{\chi,n} \approx 2 \cdot 10^{-45} \text{ cm}^2$. The atomic mass scaling factor A^2 gives an interaction cross section for xenon (assuming a WIMP mass of $m_\chi \approx 100 \text{ GeV}/c^2$) as $\sigma_{\chi,Xe} < 10^{-37} \text{ cm}^2$. This results in a total expected scattering rate in xenon of ~ 0.1 event per year per kg. This back of the envelope calculation neglects the detector efficiency ϵ , as such the number of observed events will be lower than 0.1 value for any given detector.

An important factor to consider in direct detection experiments is the annual modulation and directionality of WIMP particles towards the detector. The hypothetical Milky Way dark matter halo is modelled using the same gravitational lensing techniques which mapped the mass distribution of dark matter in the infamous Bullet

Cluster. Since WIMPs are expected to behave like a collision-less gas the velocity distribution of the halo can be assumed to follow a Maxwellian function, formulated from Boltzmann description of collision-less particles. The Milky Way dark matter halo is assumed to be in a hydro-static equilibrium between the inward gravitational force and the outwards dark matter gas pressure, with the density of dark matter varying by r^{-2} from the halo center. Measurements of the rotation curve of the Milky Way gives the local dark matter density to be $\rho_0 = 0.45^{+0.07}_{-0.09} \text{ GeV}/c^2\text{cm}^3$ (as of the Sloan Digital Sky Survey 2018 [35]). However, the value $\rho_0 = 0.3 \text{ GeV}\text{c}^2/\text{cm}^3$ is used by the detection community for consistency when comparing results. The expected scatter rate is dependent on the kinematics of moving through the halo because of the relative velocity and density distribution of WIMPs.

The average circular velocity of the sun from the galactic center V_\odot and the velocity of the earth orbiting the sun V_\oplus determine the incoming velocity V_E of WIMPs:

$$V_E = V_\odot + V_\oplus \cos(\theta) \cos(\omega[t - t_0]) \quad (1.17)$$

Annual modulation occurs because of the angular dependence of V_\oplus . When V_\oplus and V_\odot are parallel ($\cos[0]$) the incoming WIMP velocity is at a maximum and therefore a larger scattering rate is expected (see equation 1.12). Thus, the WIMP signal detection rate varies by the same relationship:

$$S(t) = B + S_0 + S_m \cos(\omega[t - t_0]) \quad (1.18)$$

Where B denotes the detector backgrounds (producing false positives). S_0 is $\approx 95\%$ larger than S_m , which means the majorly contributing component of the signal is not annually modulated [36].

1.2.4 Signal Generation

The track structure through the liquid xenon is different for nuclear recoils and electron recoils. This is primarily because nuclear recoils transfer energy to neighbouring xenon nuclei generating heat. Due to the additional energy loss, there are fewer recombination events between electrons and positive xenon ions. This is an experimentally observable difference as it is directly proportional to the ionization and scintillation signals produced. The scintillation signal is referred to as the S1 signal and the ionization signal is referred to as the S2 signal. The scintillation signal is named as such to highlight that the signal is generated by emitted photons produced from excited xenon atoms de-exciting. The photons are detected by an array of photo-multiplier tubes which surround the detector chamber. The ionization signal (S2) is caused by the ionization electrons which do not recombine with neighbouring xenon ions. Instead, they are pulled via an electric drift field towards the liquid-gas phase on the surface of the xenon. A stronger extraction field then pulls the electrons into the gas phase where the secondary S2 scintillation event occurs with gaseous xenon atoms (called electro-luminescence).

As previously stated, a nuclear recoil event will cause xenon atoms to enter an excimer excited state, denoted Xe^* . The excimer atoms will de-excite via the following process causing photons to be emitted:

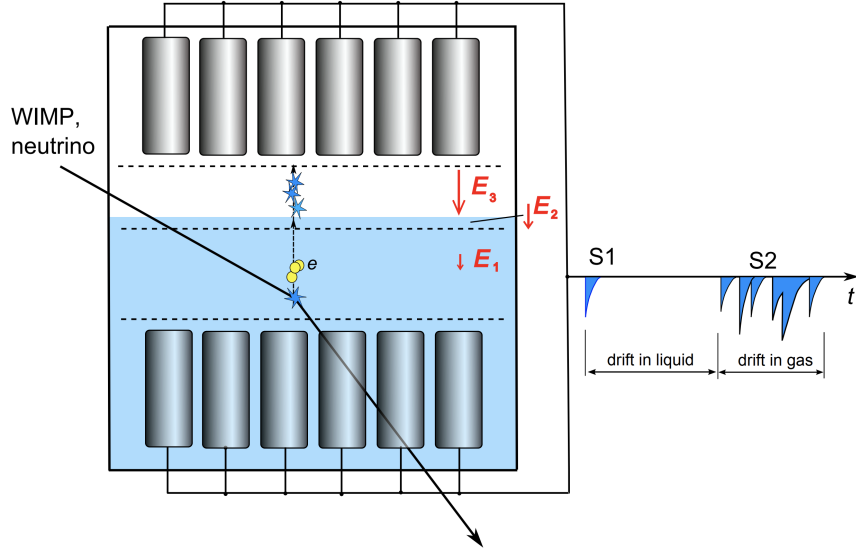


FIGURE 1.10: Cartoon illustration of a dual phase time projection chamber. Photo-multiplier tubes are arranged around the chamber and represented as cylinders. E_1 and E_3 denote the drift field and extraction field respectively. The legend gives an example of the expected pulse sizes of the S_1 and S_2 signals generated by a nuclear recoil event. It can be seen that the S_2 signal is broader due to number of ionization electrons inducing the signal. Figure acquired from [31].



The bonding of the exciton Xe^* and the xenon Xe to form a Xe_2^* dimer occurs within the order of picoseconds after the initial exciton was formed. The dimer will de-excite, emitting a ground state γ - ultra-violet photon with a wavelength of 175 nm which corresponds to $\approx 7\text{ eV}$. The de-excitation decay time constant is either 2.2 ns or 27 ns depending on if the dimer configuration is an initial singlet or triplet respectively. Both configurations contribute to the S_1 signal pulse width. Xenon's lowest ionization energy is known to be 12.1 eV, and therefore the emitted photon of 7 eV is transparent to the rest of the xenon in the chamber and can pass through the medium freely.

As well as the formation of excimers, nuclear recoils can cause the ionization of neighbouring xenon atoms. The ionization electrons are either directed towards the gas-liquid phase at the surface of the chamber by the applied electric drift field, or recombine with dimer ions to eventually form an excited state in the following process.



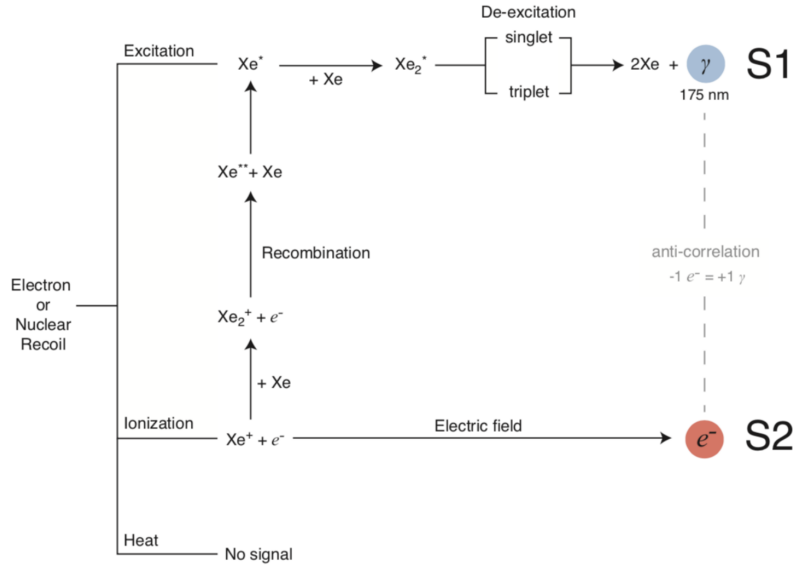


FIGURE 1.11: Schematic diagram of xenon ionization , excitation and recombination events which generate S1/S2 signals in the lZ PMTs. Figure acquired from [37].

The total S1 signal is a combination of both of the two processes defined above, however most of the photons that produce the signal originate from recombination. Electrons which escape both processes produce the S2 signal.

1.2.5 Signal Energy Scales

For any given xenon recoil (NR/ER), a number of xenon ions Xe^+ and eximers Xe^* will be produced. The number of each is denoted N_i and N_{ex} respectively. The proportion of N_i and N_{ex} produced depends on the type of recoil induced, but not on the energy of the recoil itself [38]. Dahl found that for nuclear recoils, a ratio of $N_{ex}/N_i \approx 1$ is found, while for electron recoils a ratio of $N_{ex}/N_i \approx 0.06$ is found. The length of any given recoil track is determined by the stopping power, denoted $\frac{dE}{dx}$. Nuclear recoils experience a greater stopping power resulting in shorter tracks through the liquid xenon. For reference, an energy deposit of $\approx 20\text{keV}$ via a nuclear recoil will have an approximate track length of $\approx 0.5\mu\text{m}$. An electron recoil which deposits the same amount of energy will have an approximate track length of 10nm [38].

As was stated earlier, the S1 signal is comprised mainly of photons generated through recombination, not the eximer process. This is clearly the case from the ratio of eximers to ions value of $N_{ex}/N_i \approx 0.06$.

The recombination factor r relates the number of photons produced n_γ and electrons produced n_e . The observed anti-correlation is expected since recombination requires a photon to produce an electron.

$$n_\gamma = N_{ex} + rN_i \quad (1.24)$$

$$n_e = (1 - r)N_i \quad (1.25)$$

Determining the number of electrons and photons produced for a given electron recoil is extremely useful as it allows for the recoil energy of the event to be determined through a simple calculation:

- The strength of each signal is determined by the number of photons or electrons and the signal detection efficiency, denoted g_1 or g_2 . This can be seen below:

$$S1 = g_1 n_\gamma \quad (1.26)$$

$$S2 = g_2 n_e \quad (1.27)$$

- The recoil energy deposited by a particle is given below. W denotes the required energy to create an electron/photon:

$$E_{ER} = W(n_\gamma + n_e) \quad (1.28)$$

Where $W = 13.7 \pm 0.2\text{eV}$

- Substituting the signal strengths into the energy equation gives:

$$E_{ER} = W\left(\frac{S1}{g_1} + \frac{S2}{g_2}\right) \quad (1.29)$$

The detector efficiency factors g_1 and g_2 depend on different quantities. g_1 is determined predominately by the photo-detector efficiency and geometrical light collection effects. Whereas g_2 is determined by the photo-detector efficiency and the electro-luminescence yield, Y .

As stated above, this method can only be used for calculating electron recoils. This is because in nuclear recoils a percentage of the recoil energy \mathcal{L} is dispersed as heat. The nuclear recoil energy equation must account for this and is given below:

$$E_{ER} \approx W(n_\gamma + n_e)\mathcal{L}^{-1} \quad (1.30)$$

Where \mathcal{L} is:

$$\mathcal{L} = \frac{g(\epsilon)k}{1 + g(\epsilon)k} \quad (1.31)$$

The above equation accounts for the partitioned energy from the nuclear cross section and from the electronic stopping power. The solution is an approximation of Lindhard's solution using the Thomas-Fermi model. Full details on this derivation can be found in [38, 39]. The parameter k denotes a constant of proportionality between the recoiling velocity of the struck xenon and the electronic stopping power [40].

1.3 Background Mitigation

1.3.1 General Mitigation Strategies

Reducing background material which can interfere with detection results is a continuing area of optimisation and research for direct detection experiments, this includes the LZ experiment. Sources contributing to the background can originate intrinsically within the detector or externally from the outside environment. As such, there are specific mitigating techniques to deal with each source appropriately. Some key features employed by LZ to control backgrounds are:

- The detector is placed deep underground inside an instrumented water tank. This strategy is used to mitigate cosmogenic backgrounds such as solar neutrinos.
- A large target mass of xenon to utilise self-shielding properties which originate from xenon's high density (as discussed earlier).
- The detector is made from extremely low activity radioactive materials.
- Purification of the target xenon to remove intrinsic backgrounds.
- Discrimination of the S2/S1 signals used to minimise the remaining electron recoils.
- Disregarding multiple scatter events; as a single WIMP scatter is improbable itself, a double scatter is even less likely.

Backgrounds can be split into two categories - electronic and nuclear. Gamma ray γ interactions cause electron recoils and this can be introduced externally from the environment or produced internally as decay products from radioactive isotopes found within the detector materials. One source of isotope found within the detector materials is long lived ^{39}Ar isotope, which is produced from cosmic ray activation via neutrons in the atmosphere. A strategy to mitigate exposure ^{39}Ar is to not transport components via air. Other radioactive isotopes such as ^{85}Kr , ^{137}Cs and ^{110m}Ag produced from nuclear facilities such as fuel recycling plants can be found within detector materials. As such, it is extremely important to screen all materials and only source from uncontaminated locations.

Many methods are implemented to identify clean detector materials:

- γ -spectrometry: An experimental technique to measure the γ -activity of equipment or materials. An example of the data it can produce is seen in figure: 1.12. The technique's drawback is the inherent long measuring times.
- Rn-emanation: This method involves collecting the daughter decay products of ^{222}Rn (^{218}Po and ^{214}Po) on a 'PIN-diode'. On the diode the daughters undergo an α -decay which can be easily measured and used to determine ^{222}Rn concentration.
- Neutron activation analysis: Detector materials are irradiated by neutrons which then generate characteristic γ -lines in radioactive isotopes which can be measured in γ -spectrometers.

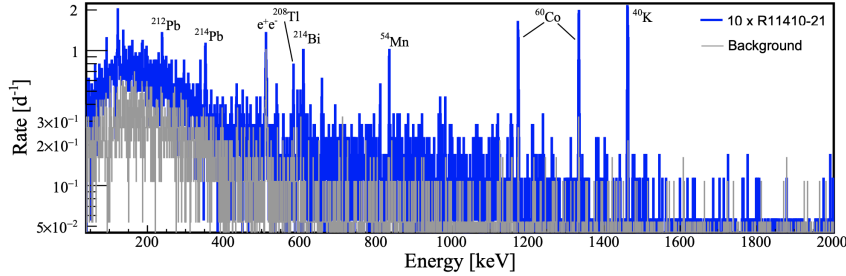


FIGURE 1.12: A γ radioactivity spectrum of the low-background photomultiplier tubes used in the LXe time projection chamber. Figure acquired from [18].

The most likely intrinsic radioactive isotope is ^{222}Rn , which is mainly produced from uranium ^{238}U and thorium ^{232}Th decay chains. A particularly challenging case of ^{222}Rn background discrimination is within the radon progeny plating the lateral PTFE (polytetrafluoroethylene) component. A ^{222}Rn decay in this location can cause minute S2 signals since electrons in close proximity to the PTFE become trapped [41]. This occurs because the β -decay products of the ^{222}Rn daughter nuclei ^{214}Pb to the ground state of ^{214}Bi can result in a single scatter electronic recoil event in energy range of the WIMP parameter search space. This is possible when the ground state decay to ^{214}Bi is not followed by a γ -emission. α -decays are less problematic as they cause a large energy deposit inside of the detector which can be easily identified and neglected.

Nuclear recoil backgrounds are of concern since they can mimic signals which would be indistinguishable from true WIMP interactions. Nuclear recoils are most likely to be caused by alpha decays from the Uranium and thorium decay chains or from elastic scattering of neutrons.

Radiogenic neutrons created via α -decays where an α particle is absorbed by a xenon nucleus thereby knocking out a neutron can cause problematic nuclear recoils. A prime candidate for this type of background is the $^{241}\text{AmBe}$ source which is used to calibrate the detector. Cosmogenic neutrons produced via relativistic muons with energies $> 40\text{GeV}$ can penetrate depths of $> 100\text{m.w.e}$ (meters water equivalent) and thus can interfere with the detector. In order to mitigate these neutrons shielding mechanisms are employed. An effective shielding method is to surround the detector with high hydrogen content material such as water, paraffin or polyethylene which can absorb neutrons. To reduce the muon intensity to below the level of radiogenic neutrons, a depth of a few hundred meters water equivalent is required [42].

Cosmogenic backgrounds (neutrinos) are insignificant at LZ due to the 4,300 m depth of the Davis Cavern where the chamber is located and water tank insulation surrounding the chamber. Muons found crossing the water tank are easily identified via Cherenkov emission and their energy deposits can be neglected. Several photomultiplier tubes are placed within the water tank to identify any muons which do in fact penetrate into the cavern. Any recorded event from these outer PMTs can be identified and neglected, as to not interfere with actual rare-event measurements.

As mentioned previously, one of the analysis techniques used to discriminate against

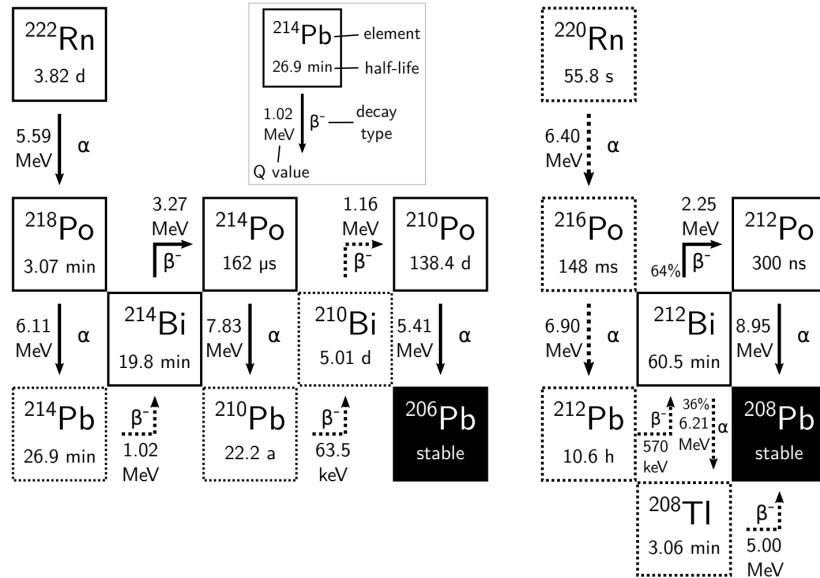


FIGURE 1.13: Graphical illustration of Radon and Thoron decay chains down to their stable isotopes. Figure acquire from [43].

backgrounds is the S1/S2 ratio. This is necessary, as even with the multitude of prevention and shielding measures, some background is still present in the fiducial volume. Taking this ratio allows one to distinguish electron recoil events from nuclear recoil events (A WIMP or otherwise). From this ratio two separate but overlapping bands named the ER band and NR band can be defined. The separation between the two bands is a result of a greater number of recombination events (between electrons and xenon ions) for nuclear recoils than for electron recoils. This means the S1 signal is amplified compared to the S2 signal. To remove up to 99.6% of all ER events, only the lower percentile of the NR band can be included when categorising a rare scatter event (although other more complex analysis methods have been developed).

1.3.2 Background Mitigation Review of LUX

The LUX experiment uses a 370 kg target of liquid xenon (LXe) to detect WIMP induced nuclear recoils. The LUX search space ranges between 3.4-25 KeV_{nr} (the subscript nr denotes that the energy deposit was caused via nuclear recoil). For a WIMP mass of ≈ 100 GeV and assuming the standard halo model of dark matter (see section xXx), the LUX detector covers 80 % of the expected WIMP interactions [44].

The dominant background for the LUX detector are electronic recoils caused by EM (electromagnetic) interactions. These interactions are primarily from photons or electrons entering the detector search space. The most likely source are the γ -rays. The calibrated background energy range of electronic recoils is given to be 0.9-5.3keV_{ee}. This overlaps the nuclear recoil energy range of 3.4-25keV_{nr} on the lower extreme of the range. Categorising events in this energy region can therefore be problematic. This is because the energy deposit could be either a WIMP induced nuclear recoil or a background ER event; the detector only has access to the energy deposit and thus cannot

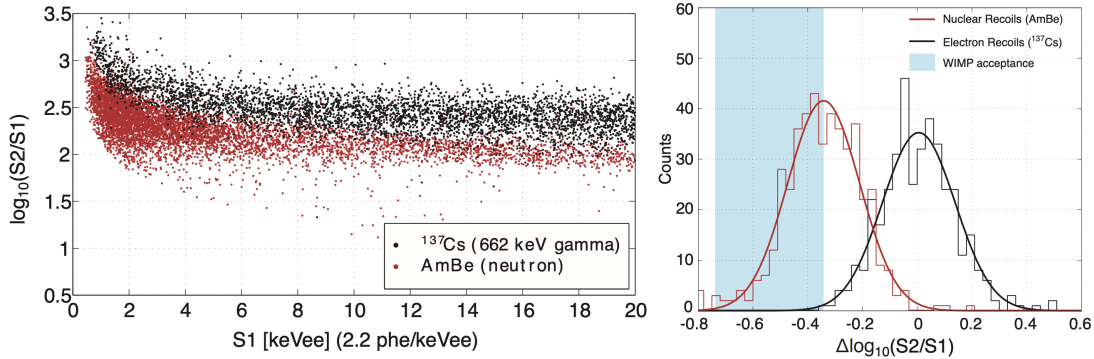


FIGURE 1.14: Nuclear recoils have a greater recombination fraction r than ER. This higher fraction allows for discrimination between the two using the S_1/S_2 signal. The two distinctive ER and NR bands can be seen on the right. The lowest fraction of the NR band is used in the WIMP search to avoid leakage from the ER band. Figure acquired from [37].

distinguish between them. One solution is to impose a direct cut to remove all events ≤ 3.4 keV, however LUX now employs a probability distribution technique to assign a likelihood to whether the energy deposits in this region are from NR or ER. This approach is preferable as you are accessing more of the event space and increasing the likelihood of detecting a WIMP over the run time. Multi-scatter (MS) events can be identified and rejected. The position of an individual scatter vertex can be found using S_1 and S_2 characteristics within an accuracy of cm in the XY plane and mm in the Z plane.

The background at LUX has been modelled via Monte Carlo simulation using the Geant4 LUXSim package [45, 46]. The simulations allow projections of the measured low energy backgrounds to be made. LUXSim enables a full reconstruction of the detector via Computer-aided design (CAD). The CAD design includes the water shielding which results in a precise model of γ -rays and neutron scattering inside the detector [44].

LUXSim includes a custom physics process package NEST (Nobel Element Simulation Techniques) which enables simulations of electronic and nuclear recoil events. This means scintillation events from photons and ionization electrons can be reproduced in the fiducial region and S_1/S_2 waveforms can be generated. However, it is also possible to only record energy deposits and still obtain S_1/S_2 waveforms without the modeling and tracking of ionization and scintillation signals.

The simulated γ -ray radiation spectra have been compared to measured real values from the detector materials to provide a more accurate estimate of the amount of radioactive materials such as ^{238}U , ^{232}Th , ^{40}K and ^{60}Co inside of the detector. To obtain the best fit to the measured γ -ray spectrum, the decay rate of each previously named radioactive isotope was varied in isolation. The results from the simulated and measured data show a high precision of agreement as can be seen in figure 1.15. There is a notable exception at 969 keV, produced from ^{228}Ac via the ^{232}Th decay chain. The simulated data predicts a 50% excess in energy. Attempts to fit the 969 keV peak cannot be found without conserving the relationship at lower and higher energies [44]. Fortunately, the

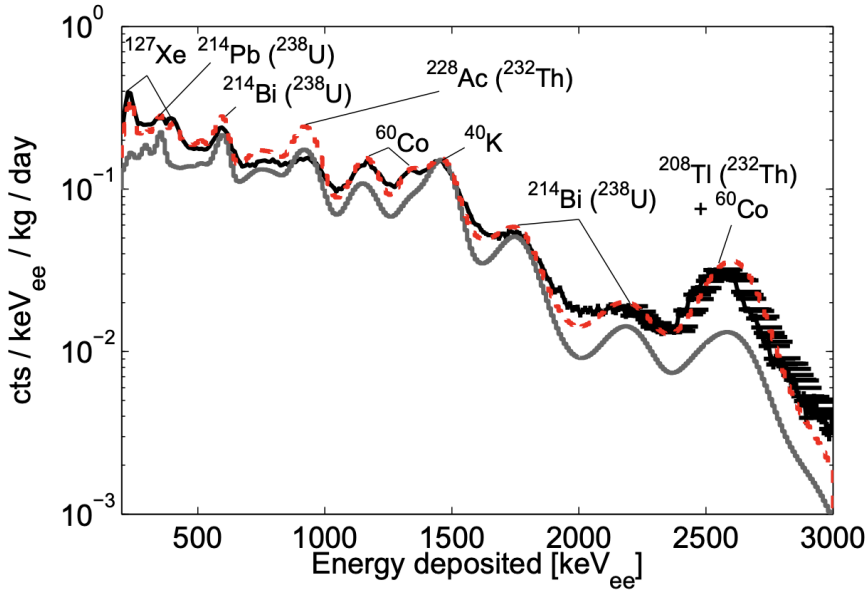


FIGURE 1.15: Comparison of simulated γ -ray spectrum modelled from LUXSim (red dotted) and the measured γ -ray spectrum (black) in the Lux fiducial volume. Energy deposits were reconstructed using S1/S2 signals, both single scatter and multi-scatter events were included. At higher energies there is a much large systematic uncertainty visible from the horizontal error bars. Figure acquired from [44].

excess does not affect γ /neutron background modeling in the WIMP search parameter space, and can therefore be ignored. The predicted concentration of ^{238}U , ^{232}Th , 40K and ^{60}Co is found to be within 1σ of what was expected by the material screening.

Radon (^{222}Rn and ^{220}Rn) daughters produce low energy electronic recoil backgrounds. Figure 1.13 shows the decay chains for both isotopes and denotes their respective short-lived half-lives for each daughter nuclei. ^{222}Rn and ^{220}Rn produce ^{214}Pb and ^{212}Pb daughters respectively. It is these particular isotopes which have ‘naked’ or ‘semi-naked’ β -decays branches. A naked β -decay results in the radiation of an β particle with no electromagnetic partner γ -particle. In contrast, semi-naked β -decays are partnered with a high energy γ -emission. The emission of a γ -ray in the semi-naked decay enables the tagging of the background event. It is however possible for the γ -ray to bypass the fiducial region, therefore resulting in the particular decay not being tagged as a background event. It is possible to identify a Radon daughter decay by the initial α -decay mode. The α -decay energy for ^{222}Rn and ^{220}Rn to ^{218}Po and ^{216}Po is 5.59 MeV and 6.40 MeV respectively. These large energy deposits are easily resolved in LUX data due to their large S1 signals which can reach up to 9×10^4 photo-electrons (phe) and this particular decay chain is the only source of α -radiation in LUX. Comparatively a S1 signal from a γ -ray produces up to only 1.5×10^4 photo-electrons. Hence, this large energy deposit signature allows for the discrimination of Radon decays.

This is a useful fact for distinguishing the naked β -decays of ^{214}Pb and ^{214}Bi which have no accompanying γ -ray emission. Although the naked decays are not directly detectable, an upper limit can be placed on their decay rates due to the measured parent

α -decays. The α decays of ^{218}Po and ^{214}Po which respectively precede and proceed the ^{214}Pb and ^{214}Bi decays yield a range of 3.5-14 mBq in the fiducial volume. The isotope ^{212}Pb has 11-hour half-life which further removes the isotope from the fiducial region and has an upper bound of <2.8 mBq from ^{216}Po [44]. The isotope ^{214}Bi can also be majorly neglected as a low energy electronic recoil background because the daughter nuclei ^{214}Po has a 160 μs half-life which will overlap with the α -decay of the daughter ^{214}Po 90% of the time. This leaves the predominate low energy electronic background to be the ^{214}Pb decay to ^{214}Bi .

Decay Chain	Isotope	Energy [MeV]	Measured Energy [MeV]	Half-life	Event Rate [mHz]
^{238}U	^{222}Rn	5.59	5.59 ± 0.08	3.8 d	17.9 ± 0.2
	^{218}Po	6.16	6.12 ± 0.10	3.1 min	14.4 ± 0.2
	^{214}Po	7.84	7.80 ± 0.2	160 μs	3.5 ± 0.1
	^{210}Po	5.30	5.22 ± 0.09	140 d	14.3 ± 0.2 (on walls) 7.2 ± 0.2 (on cathode)
^{232}Th	^{220}Rn	6.41	6.47 ± 0.09	56 s	2.6 ± 0.1
	^{216}Po	6.91	6.95 ± 0.1	0.15 s	2.8 ± 0.1
	^{212}Bi	6.21	6.12 ± 0.10	61 min	14.4 ± 0.2
	^{212}Po	8.83	—	0.30 μs	—

FIGURE 1.16: Data generated for Radon daughters from the LUX 85.3 day WIMP search run. The quoted energies relate to the Q-value for each decay which can be compared with the measured energies form the run for a sense of accuracy. Figure acquired from [44].

2

Analysis

2.0.1 Aim of Project

The focus of the proceeding chapter is the review and discussion of the undertaken independent research. The research aims to investigate the feasibility of identifying radon decays in the LZ detector, by analysing the energy deposits of the decay products down the decay chain. This is achieved by first using a Monte Carlo truth study of background Pb decays, with the objective of determining the feasibility of identifying separate energy deposit clusters associated with each decay product. If resolvable, it is expected that mono-energetic lines associated with the Bi daughters can be recovered from the detected pulses. If this is found to be true, then it may be possible to tag Pb decays in-situ, which could likely lead to improvements in measuring problematic backgrounds, measuring flow patterns in the fiducial volume and identifying earlier Rn222 decays.

2.1 Monte Carlo Truth Study of $^{214}/^{212}\text{Pb}$ Decays

2.1.1 Background

Monte Carlo Simulations are computational algorithms that utilise repeated random sampling to generate probabilities for a range of potential outcomes. The simulations work by assigning a probability distribution to various outcomes for fixed inputs. Simulated data provides a useful method to check analysis techniques quickly without having to run the detector. Another benefit of using simulated data specifically for problematic radioactive background decays is that the isotope does not have to be directly introduced inside the detector. This is particularly important for long lived isotopes such as ^{222}Rn with a half-life of 3.82 days, as the detector would be unable to record accurate data for a significant period of time after its introduction.

PMTs can only detect energy deposits and their location inside of the detector, the goal of the truth study was to find if it was feasible to reconstruct the energy deposits caused by the β -particle and the deposits caused by the ^{214}Bi . The truth data allows you to follow each energy deposits track ID and parent track ID, which enables you to trace the decay chain back to its source (β/Bi). In an actual run of the detector this would not be possible, but for the truth data it allows you to see the clustering of the energy deposits originating from each source. This is useful as it allows one to test if this technique would be viable in practice. The first analysed batch of MC truth data was for ^{214}Pb decays products from the ^{222}Rn decay chain (see figure: 1.13). The decay mode has 5 possible end point states for ^{214}Bi and a Q-value of 1019 KeV. When the

end point energy is not equal to the Q-value, the daughter Bi is produced in one of the 4 excited states (a semi-naked decay). Semi-naked decays are accompanied by a (series of) γ -ray emission(s) which cause a cascade of further energy deposits in the detector which are traced back to the Bi. The accompanying β -particle also induces its own energy deposit cascade which can be traced back to it. The β -decay equation for ^{214}Pb is below:

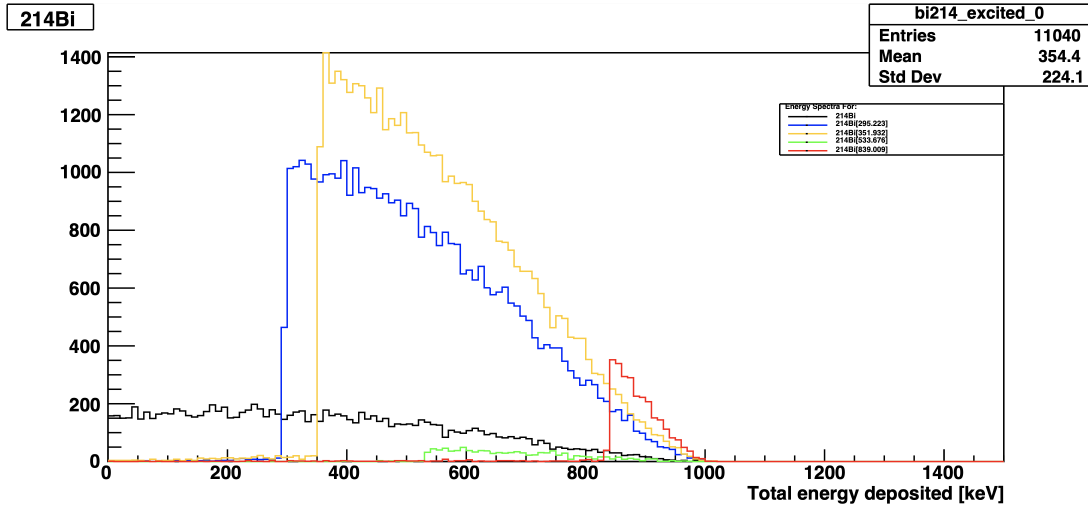


FIGURE 2.1: The legend denotes the colour code for each excited Bi state. The Q-value of 1019 KeV can clearly be seen on the x-axis. The total amount of decays to each excited state correctly represents the appropriate intensities given in table 2.1. This indicates the truth data is accurately modeling ^{214}Pb decays and that algorithm is identifying them correctly.

Figure 2.1 shows a histogram for the total energy deposited for each excited state of ^{214}Bi produced in the truth study. The Q-value of 1019 KeV indicates that a fraction of the energy is escaping detection by the PMTs the majority of the time. This is likely due to the weakly interacting antineutrino escaping the detector and carrying away energy. The slope for each decay is approximately the expected beta decay continuous energy spectrum, and with a greater sample size it is expected that this would be confirmed. The maximum count for each excited state is the case where the total amount of energy deposited in the detector is roughly equal to the energy of the excited ^{214}Bi state produced. This is due to the γ -ray emission produced from the de-excitation of ^{214}Bi , producing ionization electrons which are then likely to be detected. The small fraction of non-zero counts for when the energy deposited is less than the energy of the excited ^{214}Bi could be due to the non-zero chance that the γ -ray escapes the detector.

2 ¹⁴ Pb β -Decays Branches			
Energy (KeV)	End Point Energy (KeV)	Intensity (%)	2 ¹⁴ Bi-Daughter States
48.3	180	2.75	2 ¹⁴ Bi[839]
143.1	485	1.04	2 ¹⁴ Bi[534]
205.5	667	45.9	2 ¹⁴ Bi[352]
225.6	724	40.2	2 ¹⁴ Bi[295]
334.9	1019	11.0	2 ¹⁴ Bi

TABLE 2.1: Branched decay data for ^{214}Pb . β^- -decay intensity: 100%. Q=1019 KeV. Daughter ^{214}Bi products are shown in the final column. The final entry shows the naked β -decay to the ground state.

2.1.2 Feasibility to Tag Excited States

The weighted energy-positions for each cluster of energy deposits associated with the Bi cascade and β -particle cascade were calculated for each independent axis (x,y,z) using:

$$r_{E,x} = \frac{\sum E_D \cdot r_x}{\sum E_D} \quad (2.2)$$

$$r_{E,y} = \frac{\sum E_D \cdot r_y}{\sum E_D} \quad (2.3)$$

$$r_{E,z} = \frac{\sum E_D \cdot r_z}{\sum E_D} \quad (2.4)$$

The calculated distances are then normalised to center on the energy weighted position of the Bi induced energy deposits to show the absolute separation between the Bi cluster and the β -cluster.

$$R_{E,x} = r_{(E,x,Bi)} - r_{(E,x,\beta)} \quad (2.5)$$

The absolute separation between both clusters for 100000 events were projected onto the z-axis, x-y plane and in 3D space, as shown below:

Figures 2.2-2.4 show that the vast majority of distances fall in the <30 mm bin. Also, the mean separation difference is significantly lower in the z axis. However, because there exists a measurable mean separation in the z axis, the electrons produced from each daughter track should be separable in reconstructed space. This is possible because the drift speed of electrons to reach the PMTs arrays will allow for a measurable separation in time between the deposits. Given that the nominal drift field at LZ is 310 V/cm, the drift velocity data from the EXO-200 Detector run suggests that the drift velocity of electrons should be ≈ 1.6 mm/us [47]. The mean separation of 9.57 mm and max separation of 17.25 mm between energy deposits in the z axis gives separation times of 5.98 us and 62 us respectively. The typical width of a S2 pulse is 2-4 us. This will result in the LZAP software being able to detect separable peaks for ^{214}Pb decays, each associated with a particular cluster of energy deposited, produced from either the Bi or the β .

The same truth study was done for ^{212}Pb decays. As before, a histogram was generated to view the distribution of total energy deposited inside of the detector.

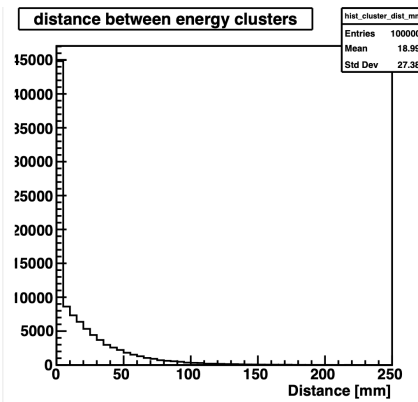


FIGURE 2.2: Results for ^{214}Pb decays. The x-axis shows the bins of the normalised absolute separation between the mean energy weighted positions of Bi associated energy deposits and β associated energy deposits.

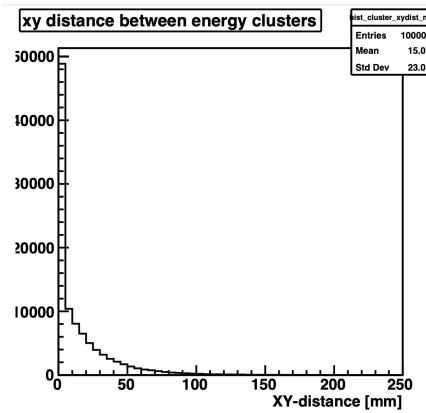


FIGURE 2.3: Results for ^{214}Pb decays. The x-axis shows the bins of the x-y projected separation between the mean energy weighted positions of Bi associated energy deposits and β associated energy deposits.

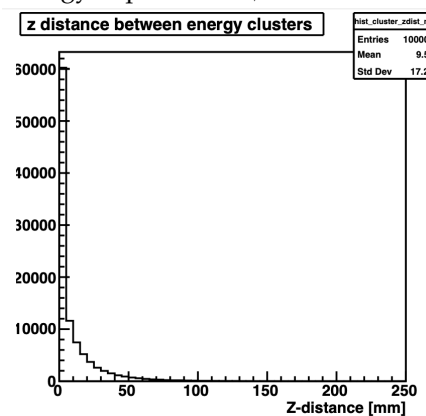


FIGURE 2.4: Results for ^{214}Pb decays. The x-axis shows the bins of the z projected separation between the mean energy weighted positions of Bi associated energy deposits and β associated energy deposits.

FIGURE 2.5

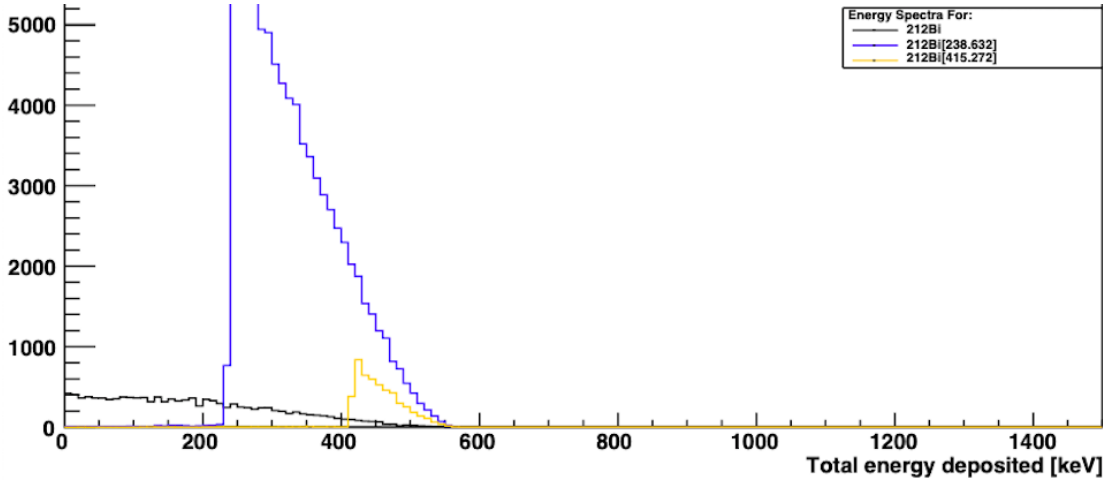


FIGURE 2.6: The legend denotes the colour code for each excited Bi state. The Q-value of 569.1 is clearly seen on the x-axis. The % of total decays to each excited state correctly represents the intensities given in table 2.2. This indicates the truth data is accurately modeling ^{212}Pb decays and the algorithm is identifying them correctly.

^{212}Pb β -Decays Branches			
Energy (KeV)	End Point Energy (KeV)	Intensity (%)	^{212}Bi -Daughter States
40.88	153.8	5.01	$^{212}\text{Bi}[415.3]$
93.28	330.5	81.5	$^{212}\text{Bi}[238.6]$
171.40	569.1	13.7	^{212}Bi

TABLE 2.2: Branched decay data for ^{212}Pb . β^- -decay intensity: 100%. Q=569.1 KeV. Daughter ^{212}Bi products are shown in the final column. The final entry shows the naked β -decay to the ground state.

The weighted energy separation between both clusters was calculated using the same method that was used for the ^{214}Pb study. The results for 100000 events are presented below. The distance was again projected into the z-axis, the x-y plane and 3D space.

Figures 2.7 - 2.9 show the results for the ^{212}Pb separation study. The mean distance separation in 3D space was 7.859 mm. This separation is approximately 2.5x smaller than the mean separation for the ^{214}Pb results. The mean separation in the z-axis projection is 3.937 mm. This is 4.4x smaller than the mean separation for the ^{214}Pb results. The difference in separation difference is due to the difference in energy of the γ -rays emitted by the excited Bi states. An excited ^{214}Bi has a higher probability of emitting a higher energy γ than an excited ^{212}Bi . Higher energy γ -rays have a smaller interaction cross section and therefore will travel further on average before interacting. Using the same electron drift velocity as determined by the EXO-200 Detector data, the mean separation in time between pulses is expected to be approximately 2.46 us. The typical width of an S2 pulse is 2-4 us, therefore, discrimination between pulses in reconstructed space should be more challenging for ^{212}Pb than ^{214}Pb , due to the smaller time

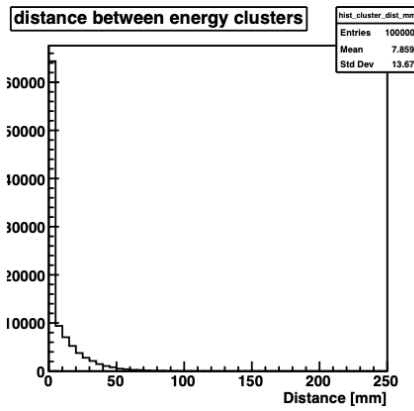


FIGURE 2.7: Results for ^{212}Pb decays. The x-axis shows the bins of the normalised absolute separation distance between the Bi cluster and the β cluster.

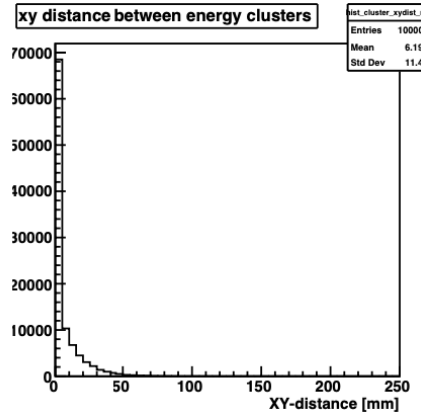


FIGURE 2.8: Results for ^{212}Pb decays. The x-axis shows the bins of the x-y projected normalised absolute separation distance between the Bi cluster and the β cluster.

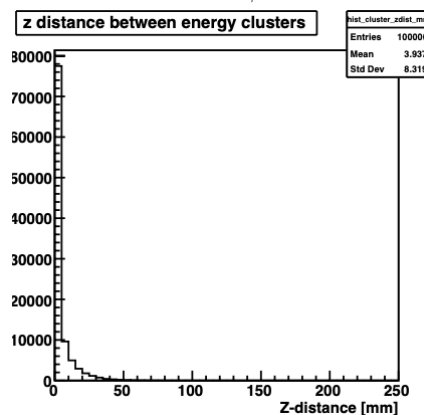


FIGURE 2.9: Results for ^{212}Pb decays. The x-axis shows the bins of the z projected normalised absolute separation distance between the Bi cluster and the β cluster.

FIGURE 2.10

separation. It is expected that reconstructed pulses from ^{212}Pb decays may often have significant overlap. But, all variables considered, it was expected that further analysis techniques could help distinguish and separate the pulses to some degree.

2.2 Analysis of Reconstructed Quantities

2.2.1 LZ Event Viewer

The LZ Offline event viewer uses BACCARAT to produce detailed simulations of events in the detector (i.e. background decays and WIMP scatter events). LZAp can accurately simulate the physics of the PMTs response to a photon hit, producing detailed digitised wave-forms which are presented in an identical format to real LZ data. LZAp reads the charge and time information acquired from the PMTs and applies pulse calibration algorithms to search for identifiable pulses. These pulses include S1/S2 signals, single electrons, multiple electrons and single photon-electrons. The PMTs also have a dark current, which is to be expected. A dark current is where the PMT produces a small amount of current output in the total absence of light. The dark count pulses are approximately the same pulse width as single photo-electron hit. The dark rate should not be thought of as a background, but as a limiting factor in the detectivity of a PMT. The PMTs also experience after-pulsing. This effect occurs in two situations, after a true photon hit and after the ionization of residual gas found in the PMT. There is often a significant time separation between the true pulse and the after-pulse, which allows them to be identified and rejected.

The pulses shown in figure 2.15 are from a ^{212}Pb decay. The S1 signal is produced from combination of scintillation photons originating from β -particle and the γ -ray emitted from the ^{212}Bi de-excitation. The γ -ray travels further than the β -particle and can experience multiple scatters. The speed of light is much greater than the resolution of the PMTs, which is why both contributions of light constitute a single S1 pulse. The S2 pulse(s) also have contributions from both the ^{212}Bi de-excitation γ and the β -particle. However, if the β and ^{212}Bi are at different depths in the detector, the pulses separate forming a double peak. In addition to this, the ^{212}Bi γ can scatter multiple times, depositing energy at multiple vertices. If these deposits are at different depths in the z-axis, this again will produce multiple S2 pulses.

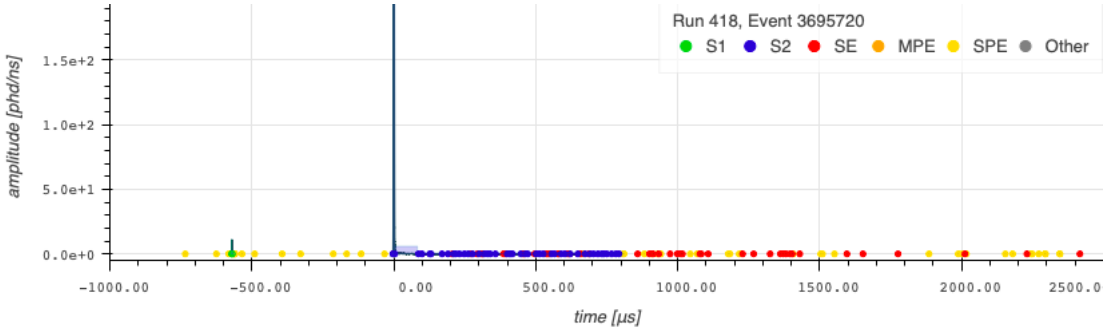


FIGURE 2.11: Example of the full LZAp event display. The S1 pulse is highlighted green, the S2 is highlighted blue.

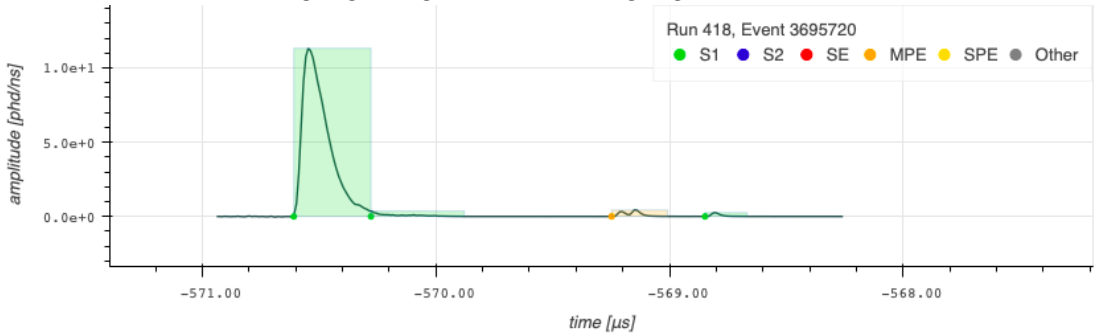


FIGURE 2.12: Highlighted S1 pulse from figure 2.11.

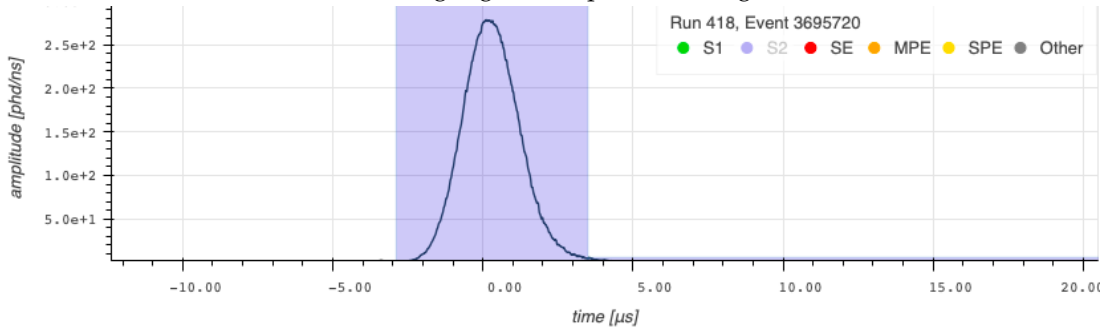


FIGURE 2.13: Highlighted S2 pulse from figure 2.11. The width of the pulse is in agreement with the predict width from the cluster separation analysis

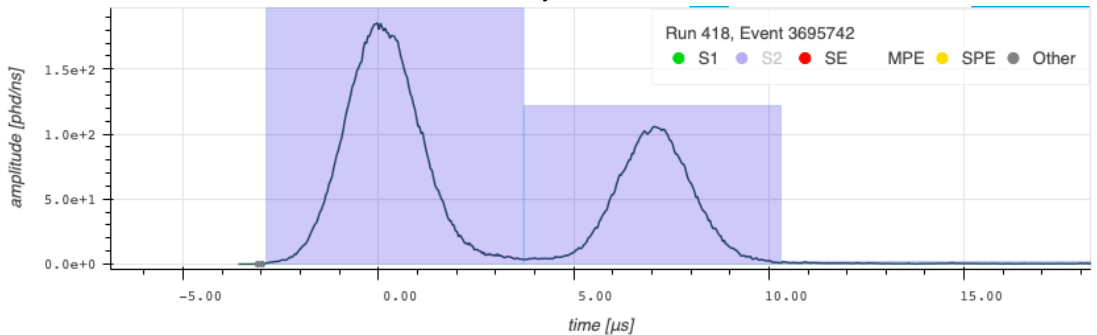


FIGURE 2.14: Example of a multi-scatter S2

FIGURE 2.15

2.2.2 Pulse Classification Performance

To see how the LZAp pulse classification algorithm performed for each categorised pulse, 2D scatter plots were made for a variety of parameters. These include top bottom asymmetry (TBA), pulse area, pulse width and pf50ns. The pulse width is the duration of the pulse measured in time. Pf50ns denotes the percentage of the pulse which occurred within the first 50 ns. It is expected that for S1 events the majority of the pulse would be within 50ns, whereas for wider S2 events which are approximately between 2-4 us, only a small fraction of the pulse would be within 50 ns. Pulse areas are given in units of phd, which are units of detected photons. Top bottom asymmetry refers to the amount of detected light in the top PMT array and the bottom PMT array. +1 denotes that all the light was detected in the top array, and -1 denotes that all the light was detected in the bottom array. Figure 2.16 shows the results for the pf50ns vs

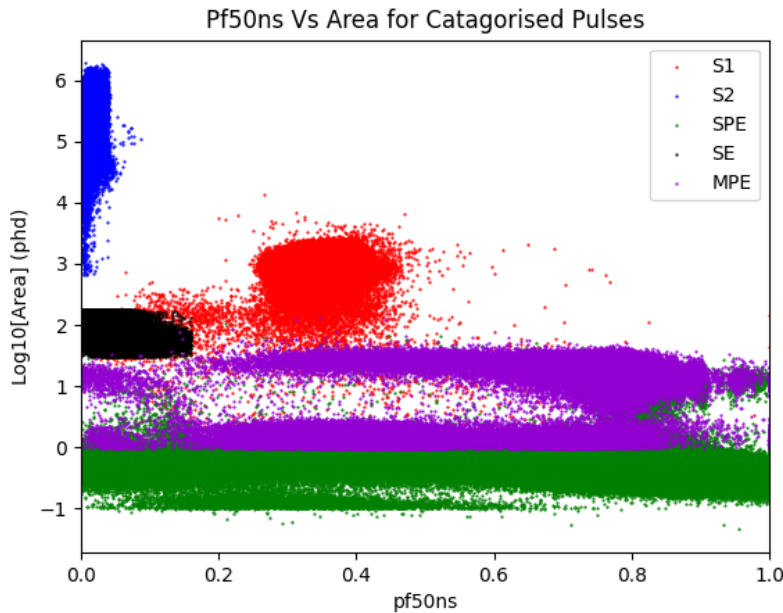


FIGURE 2.16: Scatter plot for Pf50ns vs Log₁₀[area].

pulse area plot. As expected, the S2 pulses dominate the top left quadrant of the plot, with the vast majority of pulses having <10% of their total area occurring in the first 50 ns. An interesting observation is the negative values of area for a fraction of the SPEs. This is due to a PMT recording baseline noise (which can have negative areas) at the same time as a SPE hit. Baseline noise is produces a much smaller area than a SPE hit and fluctuates around 0. This effect is also observed in the TBA plot. The S1 pulses range between 0.3-0.45 pf50ns. Therefore, 30-45% of the pulse occurs with the first 50 ns. This is expected as the S1 pulses produce sharper, narrower peaks than S2 pulses. This can be seen visually in the event display images in figures 2.12 and 2.13.

Figure 2.17 shows the results for the TBA vs area plot. 1 is equivalent to 100% of the light in the top array and -1 is equivalent to 100% of the light in the bottom array. The plot confirms that the majority of the S2 pulse is detected by the top array. This

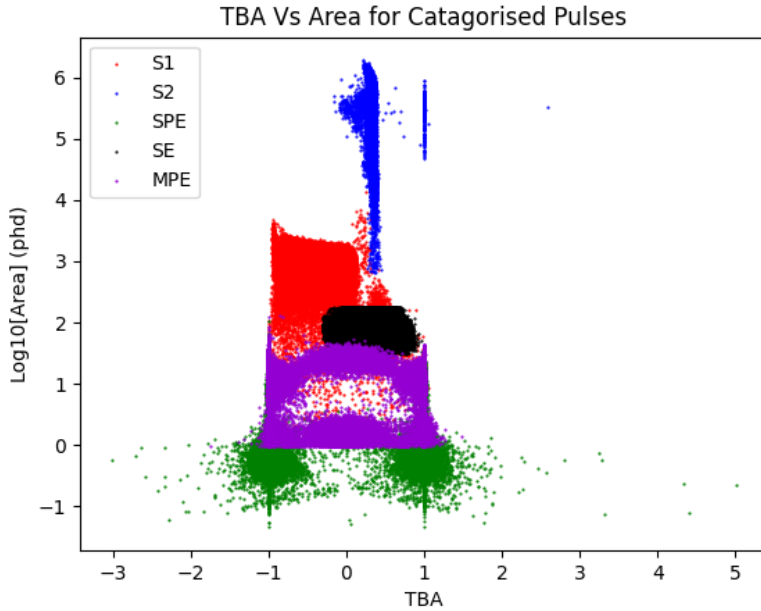


FIGURE 2.17: Scatter plot for top bottom asymmetry (TBA) vs $\text{Log}_{10}[\text{area}]$.

is expected because the drift field pulls ionization electrons towards the top array. A small number of S2 events show that almost 100% of their light was detected in the top array. This is likely due to the decay occurring near the top of the fiducial volume. As also seen in the pf50ns plot, some SPE pulses have a TBA value $> |1|$. This effect is carried over from the baseline noise in the PMTs producing negative areas, as the function to determine TBA values depends on the top/bottom pulse area.

Figure 2.19 shows the results for pulse width vs pulse area plots. Plot a) shows the first attempt results. The S2 distribution shows a large spread of widths, with significantly larger areas than other pulses. The island of S2s with $\approx 2 \cdot 10^2$ phd are highly likely to be due to a misclassification of SEs due to the LZAp pulse finding algorithm. A brute force correction cut was applied to remove these events, so not to effect further analysis. The cut was a simple function which stated any S2 with an area below the given threshold should be removed (see equation below):

$$\text{area} = 0.188 \cdot \text{width} + 624 \quad (2.6)$$

In equation 2.6, 0.188 has units of phd/ns, width has units of ns and the constant 624 has units of phd. This cut is effectively a straight line with a gradient of 0.188 and y-intercept of 624. The corrected plot can be seen in figure 2.19 b) which no longer has the island of S2 events at $\approx 2 \cdot 10^2$ phd.

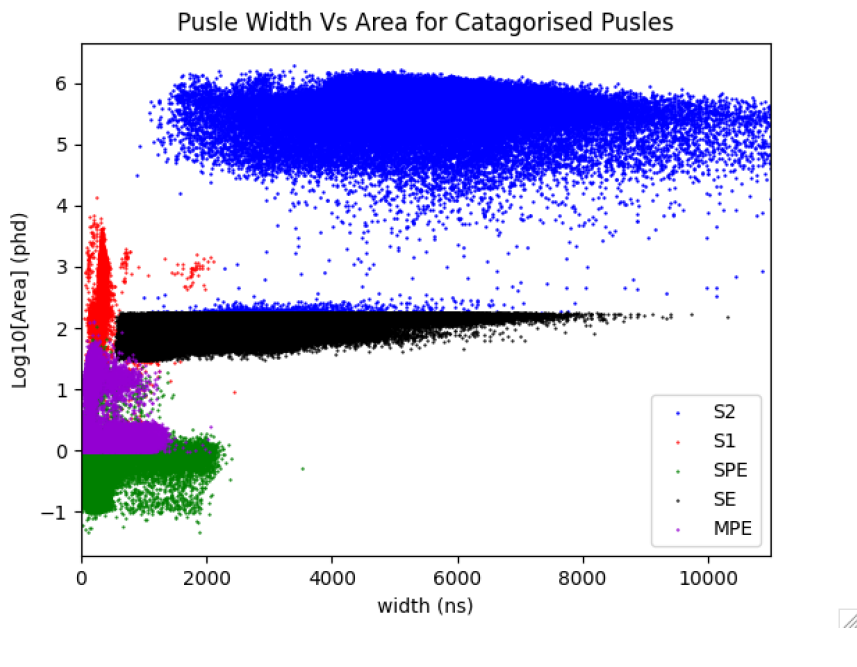
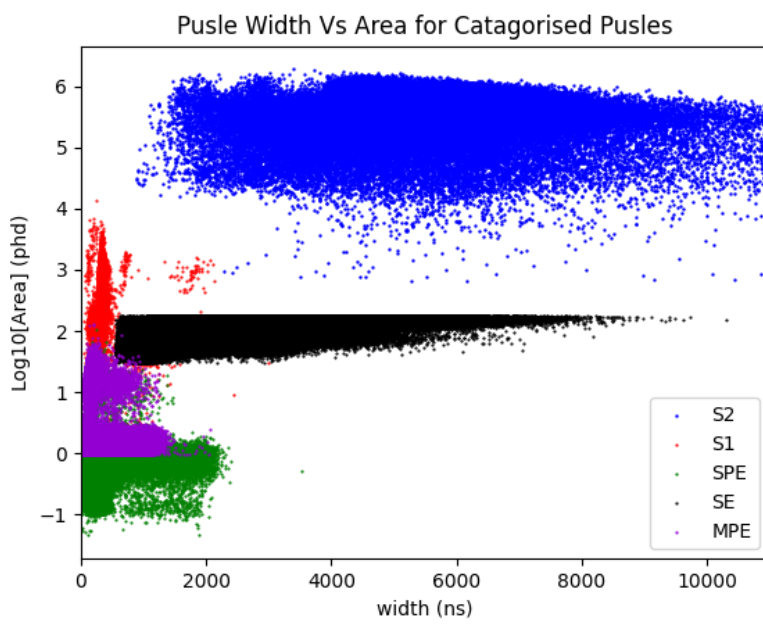


FIGURE 2.18: Scatter plot of pulse width vs $\log_{10}[\text{area}]$. A fraction of S2 pulses are being misclassified as SE pulses



(a)

FIGURE 2.19: Scatter plot of pulse width vs $\log_{10}[\text{area}]$. A cut has been applied to remove the misclassified S2s

2.2.3 Event Selection

The ^{212}Pb data-set contained 142809 events. Each event corresponds to one window in the LZ Offline event viewer as seen in figure 2.15. The first step was to develop an event selection algorithm to identify and count S1 and S2 pulses for each event. It is possible for the LZAp pulse finding algorithm to misclassify pulses as true S1/S2s, conditions (called cuts) need to be made to reduce the probability of including the incorrectly categorised events. An example of such a cut would be to find the maximum area of a S2 during one event window and call this the ‘true’ S2, and any categorised S2 with a pulse area smaller than 5% of the ‘true’ S2 area is removed. The pulse area is used as it corresponds to the strength of the signal produced in the PMT. This same condition also applies to the S1 pulse, but a 10% area cut is applied instead. The reason for this is that S2 pulses have a much larger area than S1 pulses. The performance of the classification algorithm is presented in the table below:

Event Classification for ^{212}Pb Decays	
Classification	Frequency
Single-Scatter	63871
Multi-scatter	22990
Single S1	8425
Single S2	200
No Pulses	45852
Pile Up	1471
Total	142809

TABLE 2.3: Performance of the event classification algorithm with maximum area threshold cuts applied for 142809 events. Pile up consists of events with multiple S1 and S2 pulses. No pulse consists of events with no S1 or S2 pulses. Multi-scatter consists of events with one S1 and more than one S2.

Table 2.4 shows the breakdown of S1 and S2 events for the ^{212}Pb data set. 32.1% of events are not registering any S1 or S2 pulses. These events are likely to be consisting of SPE, SE and MPE events or events in the outer detector/skin. The most common event occurring 44.72% of the time is a single scatter consisting of 1 S1 and 1 S2 pulse, with the second most common being multi-scatter events occurring 16.10% of the time. The multi-scatter category consists of 1 S1 and S2 events, which occur 10.6% of the time, which is to say that 66.0% of multi-scatters are 1 S1 and 2S2s (see figure 2.14). These

Event Classification Percentage Matrix for ^{212}Pb Decays			
	0 S1	1 S1	>1 S1
0 S2	32.1%	5.88%	0.02%
1 S2	0.08%	44.72%	0.93%
>1 S2	0.06%	16.10%	0.10%

TABLE 2.4: The matrix shows the percentage groupings of S1 and S2 events.

multi-scatter 1 S1 2 S2 events are to be used in the attempt to identify the ^{212}Pb decays in the detector.

2.2.4 Tagging Decays from Reconstructed Data

To attempt to tag the ^{212}Pb decays, 1 S1 2 S2 multi-scatter events were analysed. The first step was to plot the area of the first S2 pulse against the area of the second S2 pulse. This can be seen in figure 2.20. A symmetry is found along the $y=x$ line. This is expected

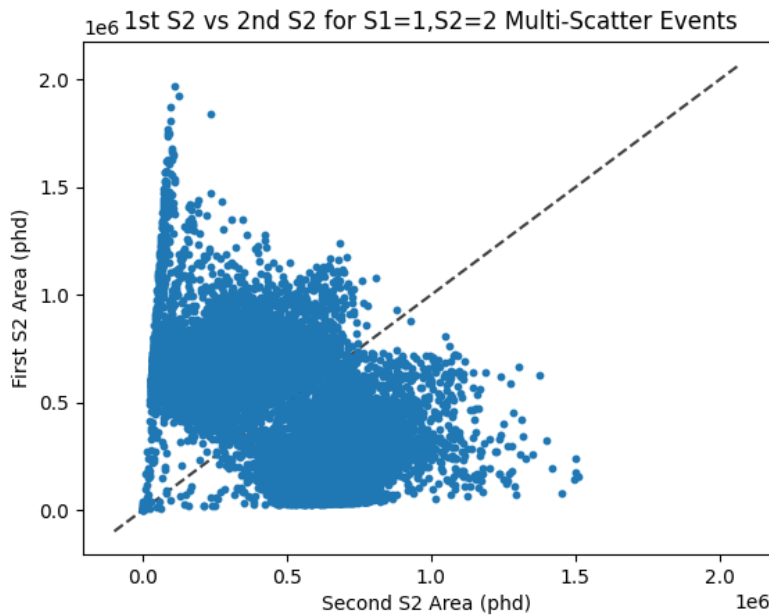


FIGURE 2.20: Scatter plot of the first S2 pulse area vs the second S2 pulse area for all events in the data set.

as the γ -emissions from the β -decay can deposit their energy at different depths in the z-axis, causing the S2 pulse to not overlap. Since there is no preferred direction, it is expected that the first S2 and second S2 pulse should look similar when averaged over all events. Figure 2.20 provides a good indicator that ^{212}Bi decays could be tagged, however, further information can be extracted from the area of both S2 pulses by replotting the areas in a histogram with a heat map overlay. This can be seen in figure 2.21. The sharp cut off in events close to the x and y axes is due to the maximum area threshold cuts described in section 2.23. Any S2 with an area below the set threshold is treated as a misclassification and removed from the data set. The symmetry along the $y=x$ line has presented itself with more clarity here. Two intense cluster features on either side of the $y=x$ have now developed. These blurred features are mono-energetic lines associated with the γ 's emitted from ^{212}Bi de-excitations.

The mono-energetic lines are most pronounced when the antineutrino from the β -decay takes a significant fraction of the energy from the decay. Neutrinos are very weakly interacting and therefore this energy is not picked up by the PMTs. Therefore, the majority of the energy deposited in the detector is caused by the ^{212}Bi de-excitation

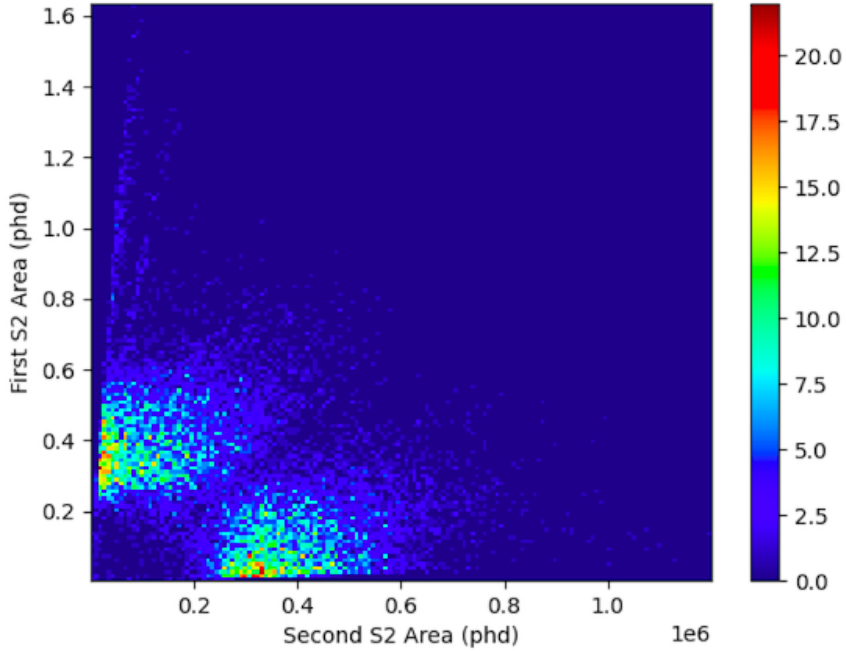


FIGURE 2.21: Histogram of the second S2 pulse area vs first S2 pulse area. The heatmap indicates the intensity of events at given areas.

γ . The features are blurred because energy deposits at lower depths in the detector result in less intense PMT pulses. This is because of the increased likelihood of recombination events associated with a longer path length. To resolve this, correction factors need to be applied to the pulses to reduce the smearing effect. The correction factor for S2 pulses depend only on the location of the energy deposit, however, the correction factor for S1 pulses depends on the drift time for the following S2 pulse and the S2 position. For multi-scatter events with 2 S2 pulses this present a problem as it is unclear which S2 pulse to use, as the S1 light is a mixture of light produced from two separate energy deposits at different positions (and therefore drift times). To attempt to resolve this issue, a S2 area weighted average of the drift time and position for each S2 pulse was used. The S2 area had to be used as a proxy for relative size of the S1 area.

Figure 2.22 is formed from the same data set that resulted in figure 2.21, but with the correction factors applied. The central location of the mono-energetic features has been translated from $\approx 3 \cdot 10^6$ phd to $\approx 6.2 \cdot 10^6$ phd. The bands have been narrowed and are now well defined. The spread around the central peak of the bands is due to the β -decay energy spectrum as the antineutrino carries away energy, meaning a range of energy is deposited in the detector for a given decay.

To further enhance the two mono-energetic lines, the S1 area was plotted against both the first and second S2 bottom areas. Using the bottom S2 area provides a higher resolution because the S2 areas are so large that they saturate the top PMTs. This can be confirmed by viewing figure 2.17 which shows the top bottom asymmetry for pulses. Since the bottom PMTs detect less light, this saturation effect is avoided. The reconstruction energy can then be calculated using the central position of each cluster in

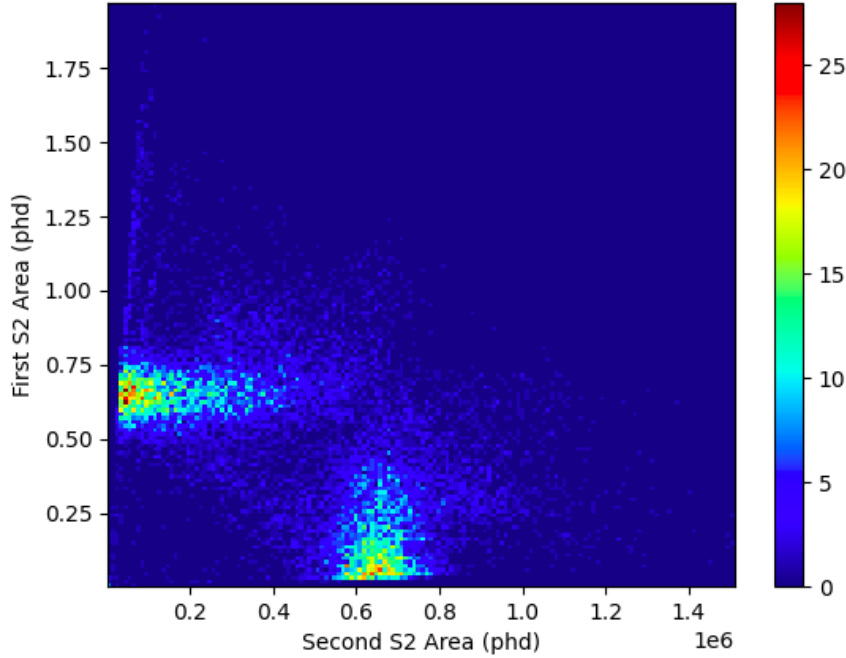


FIGURE 2.22: Histogram of the second S2 pulse area vs first S2 pulse area, with correction factors applied.

figure 2.23 using equation 1.29 derived, in section 1.2.5. For clarity the equation is restated below:

$$E = W \left(\frac{S1}{g1} + \frac{S2}{g2} \right) \quad (2.7)$$

$W=13.7$ eV, $g_1 = 0.1201\%$ phd/photon, $g_2 = 795\%$ phd/electron and $g_{2,bottom} = 245\%$ phd/electron.

Using figure 2.22, the reconstructed energy value is 228.336 KeV. This was obtained using a S1 area value of 900 phd and a S2 area value of 220000 phd. The 6% uncertainty follows from the uncertainty in the $g_{1,2}$ factors. The most common ^{212}Pb decay, occurring 81.5% of the time, is to $^{212}\text{Bi}[238.6]$ (see table 2.2) The calculated reconstruction energy is 4.3% away from this value, and therefore falls within its uncertainty.

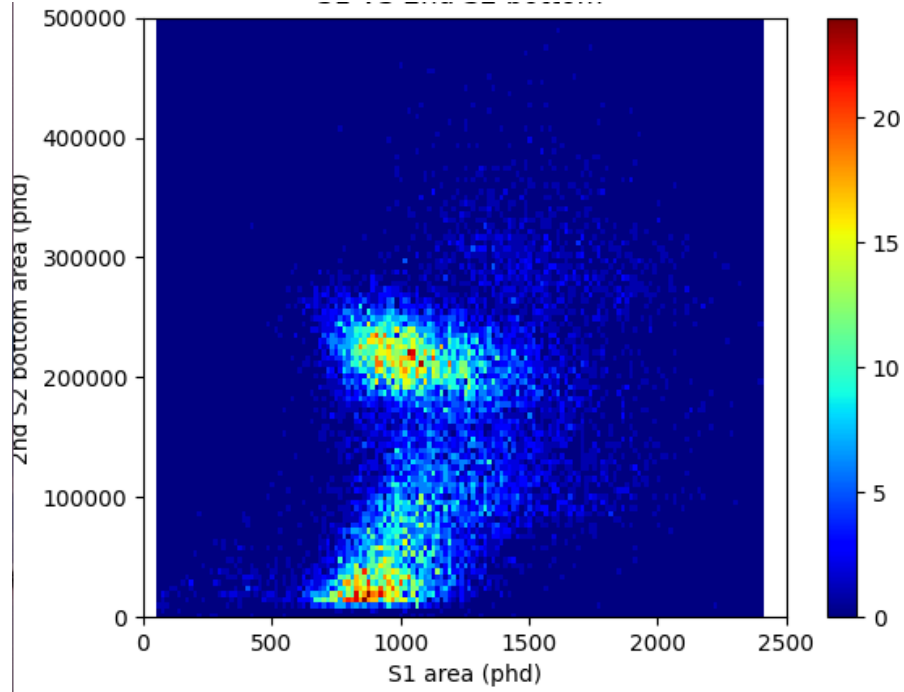


FIGURE 2.23: Second S2 pulse bottom area VS S1 area.

2.3 Conclusion

The energy reconstruction calculation in previous section demonstrates that it is possible to identify the ^{212}Bi excited state from reconstructing the pulse areas for 1 S1 2 S2 events defined by the LZAP algorithm, with the additional cuts presented in this thesis. Having shown that it is theoretically possible to calculate the mono-energetic calibration lines, further research would need to be undertaken to check that this can be done in-situ. If possible, the tagging of ^{212}Pb decays to ^{212}Bi would allow for the measurement of problematic background rates and the measurement of flow patterns of ^{212}Pb isotopes. One specific example is of the discovery of dead regions in the fiducial volume that do not participate in the purification systems.

Recalling the separation of energy deposits calculated in section 2.1.1 for ^{212}Pb decays and ^{214}Pb decays, it was shown that the separation between the energy deposit clusters was smaller for the ^{212}Pb decay. Since it was possible to derive the mono-energetic lines in this case, it is highly likely that for the ^{214}Pb isotope with larger separations due to the higher energy γ 's, the mono-energetic lines would be more defined and provide increasingly accurate results. This is encouraging because ^{214}Pb is the predominate low energy electronic background in the LZ detector. To improve the ability to find the mono-energetic lines, improvements in separating 2 S2 events in the event viewer could be made. This can be observed in events where the separation in the z axis is small, and the two S2 areas slightly overlap. To attempt to disentangle these areas, shapes could be fit to the pulses to find an estimation of both of their areas. Increasing the number of events which can be effectively tagged would enhance the ability

to measure problematic backgrounds and flows. For further development of this research, it would now make sense to check what percentage of Bi can now be identified in the truth data. Conducting this check would provide an efficiency measurement on how effective the reconstruction algorithm was.

Bibliography

- [1] R. Clausius. "XVI. On a mechanical theorem applicable to heat". In: *The London, Edinburgh, and Dublin Philosophical Magazine and Journal of Science* 40.265 (1870), pp. 122–127. DOI: [10.1080/14786447008640370](https://doi.org/10.1080/14786447008640370). eprint: <https://doi.org/10.1080/14786447008640370>. URL: <https://doi.org/10.1080/14786447008640370>.
- [2] F. Zwicky. "Republication of: The redshift of extragalactic nebulae". In: *General Relativity and Gravitation* 41.1 (2009), pp. 207–224. DOI: [10.1007/s10714-008-0707-4](https://doi.org/10.1007/s10714-008-0707-4). URL: <https://doi.org/10.1007/s10714-008-0707-4>.
- [3] Planck Collaboration et al. "Planck 2015 results - XIII. Cosmological parameters". In: *A&A* 594 (2016), A13. DOI: [10.1051/0004-6361/201525830](https://doi.org/10.1051/0004-6361/201525830). URL: <https://doi.org/10.1051/0004-6361/201525830>.
- [4] F. Zwicky. "On the Masses of Nebulae and of Clusters of Nebulae". In: 86 (Oct. 1937), p. 217. DOI: [10.1086/143864](https://doi.org/10.1086/143864).
- [5] N. J. Woolf. "On the Stabilization of Clusters of Galaxies by Ionized Gas". In: 148 (Apr. 1967), p. 287. DOI: [10.1086/149148](https://doi.org/10.1086/149148).
- [6] JOHN F. MEEKINS et al. "Physical Sciences: X-rays from the Coma Cluster of Galaxies". In: *Nature* 231.5298 (1971), pp. 107–108. DOI: [10.1038/231107a0](https://doi.org/10.1038/231107a0). URL: <https://doi.org/10.1038/231107a0>.
- [7] Frank Hohl. "Dynamics of plance stellar systems". In: *Astrophysics and Space Science* 14.1 (1971), pp. 91–109. DOI: [10.1007/BF00649197](https://doi.org/10.1007/BF00649197). URL: <https://doi.org/10.1007/BF00649197>.
- [8] A. Toomre. "On the gravitational stability of a disk of stars." In: 139 (May 1964), pp. 1217–1238. DOI: [10.1086/147861](https://doi.org/10.1086/147861).
- [9] Frank Hohl. "Numerical Experiments with a Disk of Stars". In: 168 (Sept. 1971), p. 343. DOI: [10.1086/151091](https://doi.org/10.1086/151091).
- [10] J. P. Ostriker and P. J. E. Peebles. "A Numerical Study of the Stability of Flattened Galaxies: or, can Cold Galaxies Survive?" In: 186 (Dec. 1973), pp. 467–480. DOI: [10.1086/152513](https://doi.org/10.1086/152513).
- [11] H. I. Ewen and E. M. Purcell. "Observation of a Line in the Galactic Radio Spectrum: Radiation from Galactic Hydrogen at 1,420 Mc./sec." In: *Nature* 168.4270 (1951), pp. 356–356. DOI: [10.1038/168356a0](https://doi.org/10.1038/168356a0). URL: <https://doi.org/10.1038/168356a0>.
- [12] K. C. Freeman. "Erratum: on the Disks of Spiral and s0 Galaxies". In: 161 (Sept. 1970), p. 802. DOI: [10.1086/150583](https://doi.org/10.1086/150583).

- [13] Lars Bergström. "Non-baryonic dark matter: observational evidence and detection methods". In: *Reports on Progress in Physics* 63.5 (Apr. 2000), pp. 793–841. ISSN: 1361-6633. DOI: [10.1088/0034-4885/63/5/2r3](https://doi.org/10.1088/0034-4885/63/5/2r3). URL: <http://dx.doi.org/10.1088/0034-4885/63/5/2r3>.
- [14] Katherine Garrett and Gintaras Duda. "Dark Matter: A Primer". In: *Advances in Astronomy* 2011 (2011), pp. 1–22. ISSN: 1687-7977. DOI: [10.1155/2011/968283](https://doi.org/10.1155/2011/968283). URL: <http://dx.doi.org/10.1155/2011/968283>.
- [15] Henk Hoekstra et al. "Weak Lensing Analysis of Cl 135862 Using Hubble Space Telescope Observations". In: *The Astrophysical Journal* 504.2 (Sept. 1998), pp. 636–660. DOI: [10.1086/306102](https://doi.org/10.1086/306102). URL: <https://doi.org/10.1086/306102>.
- [16] Douglas Clowe et al. "A Direct Empirical Proof of the Existence of Dark Matter". In: *The Astrophysical Journal* 648.2 (Aug. 2006), pp. L109–L113. DOI: [10.1086/508162](https://doi.org/10.1086/508162). URL: <https://doi.org/10.1086/508162>.
- [17] N. Aghanim et al. "Planck 2018 results". In: *Astronomy & Astrophysics* 641 (Sept. 2020), A6. ISSN: 1432-0746. DOI: [10.1051/0004-6361/201833910](https://doi.org/10.1051/0004-6361/201833910). URL: <http://dx.doi.org/10.1051/0004-6361/201833910>.
- [18] Marc Schumann. "Direct detection of WIMP dark matter: concepts and status". In: *Journal of Physics G: Nuclear and Particle Physics* 46.10 (Aug. 2019), p. 103003. ISSN: 1361-6471. DOI: [10.1088/1361-6471/ab2ea5](https://doi.org/10.1088/1361-6471/ab2ea5). URL: <http://dx.doi.org/10.1088/1361-6471/ab2ea5>.
- [19] Ya B. Zeldovich. "The Theory of the Large Scale Structure of the Universe". In: *Symposium - International Astronomical Union* 79 (1978), pp. 409–421. DOI: [10.1017/S0074180900144882](https://doi.org/10.1017/S0074180900144882).
- [20] Scott Tremaine and James E. Gunn. "Dynamical Role of Light Neutral Leptons in Cosmology". In: *Phys. Rev. Lett.* 42 (6 Feb. 1979), pp. 407–410. DOI: [10.1103/PhysRevLett.42.407](https://doi.org/10.1103/PhysRevLett.42.407). URL: <https://link.aps.org/doi/10.1103/PhysRevLett.42.407>.
- [21] George R. Blumenthal et al. "Formation of galaxies and large-scale structure with cold dark matter". In: *Nature* 311.5986 (1984), pp. 517–525. DOI: [10.1038/311517a0](https://doi.org/10.1038/311517a0). URL: <https://doi.org/10.1038/311517a0>.
- [22] R. D. Peccei and Helen R. Quinn. "Constraints imposed by CP conservation in the presence of pseudoparticles". In: *Phys. Rev. D* 16 (6 Sept. 1977), pp. 1791–1797. DOI: [10.1103/PhysRevD.16.1791](https://doi.org/10.1103/PhysRevD.16.1791). URL: <https://link.aps.org/doi/10.1103/PhysRevD.16.1791>.
- [23] Georg Raffelt. "Axion hunting at the turn of the millennium". In: *Nuclear Physics B - Proceedings Supplements* 77.1-3 (May 1999), pp. 456–461. ISSN: 0920-5632. DOI: [10.1016/S0920-5632\(99\)00467-3](https://doi.org/10.1016/S0920-5632(99)00467-3). URL: [http://dx.doi.org/10.1016/S0920-5632\(99\)00467-3](http://dx.doi.org/10.1016/S0920-5632(99)00467-3).
- [24] C. Hagmann et al. "Results from a High-Sensitivity Search for Cosmic Axions". In: *Phys. Rev. Lett.* 80 (10 Mar. 1998), pp. 2043–2046. DOI: [10.1103/PhysRevLett.80.2043](https://doi.org/10.1103/PhysRevLett.80.2043). URL: <https://link.aps.org/doi/10.1103/PhysRevLett.80.2043>.

- [25] I. Ogawa, S. Matsuki, and K. Yamamoto. "Interactions of cosmic axions with Rydberg atoms in resonant cavities via the Primakoff process". In: *Phys. Rev. D* 53 (4 Feb. 1996), R1740–R1744. DOI: [10.1103/PhysRevD.53.R1740](https://doi.org/10.1103/PhysRevD.53.R1740). URL: <https://link.aps.org/doi/10.1103/PhysRevD.53.R1740>.
- [26] S.P. Ahlen et al. "Limits on cold dark matter candidates from an ultralow background germanium spectrometer". In: *Physics Letters B* 195 (Sept. 1987), pp. 603–608. DOI: [10.1016/0370-2693\(87\)91581-4](https://doi.org/10.1016/0370-2693(87)91581-4).
- [27] R. Bernabei et al. "First model independent results from DAMA/LIBRA-phase2". In: *Nuclear Physics and Atomic Energy* 19.4 (Dec. 2018), pp. 307–325. ISSN: 2074-0565. DOI: [10.15407/jnpae2018.04.307](https://doi.org/10.15407/jnpae2018.04.307). URL: <http://dx.doi.org/10.15407/jnpae2018.04.307>.
- [28] P. N. Luke et al. "Calorimetric ionization detector". In: *Nucl. Instrum. Meth. A* 289 (1990), pp. 406–409. DOI: [10.1016/0168-9002\(90\)91510-I](https://doi.org/10.1016/0168-9002(90)91510-I).
- [29] F. Aubin et al. "Discrimination of nuclear recoils from alpha particles with superheated liquids". In: *New J. Phys.* 10 (2008), p. 103017. DOI: [10.1088/1367-2630/10/10/103017](https://doi.org/10.1088/1367-2630/10/10/103017). arXiv: [0807.1536 \[physics.ins-det\]](https://arxiv.org/abs/0807.1536).
- [30] B. J. Mount et al. *LUX-ZEPLIN (LZ) Technical Design Report*. 2017. arXiv: [1703.09144 \[physics.ins-det\]](https://arxiv.org/abs/1703.09144).
- [31] Vitaly Chepel and Henrique Araújo. "Liquid noble gas detectors for low energy particle physics". In: *Journal of Instrumentation* 8 (July 2012). DOI: [10.1088/1748-0221/8/04/R04001](https://doi.org/10.1088/1748-0221/8/04/R04001).
- [32] Jennifer M. Gaskins. "A review of indirect searches for particle dark matter". In: *Contemporary Physics* 57.4 (2016), pp. 496–525. DOI: [10.1080/00107514.2016.1175160](https://doi.org/10.1080/00107514.2016.1175160). eprint: <https://doi.org/10.1080/00107514.2016.1175160>. URL: <https://doi.org/10.1080/00107514.2016.1175160>.
- [33] Martin C. Smith et al. "The RAVE survey: constraining the local Galactic escape speed". In: *Monthly Notices of the Royal Astronomical Society* 379.2 (July 2007), pp. 755–772. ISSN: 0035-8711. DOI: [10.1111/j.1365-2966.2007.11964.x](https://doi.org/10.1111/j.1365-2966.2007.11964.x). eprint: <https://academic.oup.com/mnras/article-pdf/379/2/755/3399611/mnras0379-0755.pdf>. URL: <https://doi.org/10.1111/j.1365-2966.2007.11964.x>.
- [34] J.D. Lewin and P.F. Smith. "Review of mathematics, numerical factors, and corrections for dark matter experiments based on elastic nuclear recoil". In: *Astroparticle Physics* 6.1 (1996), pp. 87–112. ISSN: 0927-6505. DOI: [https://doi.org/10.1016/S0927-6505\(96\)00047-3](https://doi.org/10.1016/S0927-6505(96)00047-3). URL: <https://www.sciencedirect.com/science/article/pii/S0927650596000473>.
- [35] S Sivertsson et al. "The local dark matter density from SDSS-SEGUE G-dwarfs". In: *Monthly Notices of the Royal Astronomical Society* 478.2 (Apr. 2018), pp. 1677–1693. ISSN: 0035-8711. DOI: [10.1093/mnras/sty977](https://doi.org/10.1093/mnras/sty977). eprint: <https://academic.oup.com/mnras/article-pdf/478/2/1677/25059992/sty977.pdf>. URL: <https://doi.org/10.1093/mnras/sty977>.

- [36] Andrzej K. Drukier, Katherine Freese, and David N. Spergel. "Detecting cold dark-matter candidates". In: *Phys. Rev. D* 33 (12 June 1986), pp. 3495–3508. DOI: [10.1103/PhysRevD.33.3495](https://doi.org/10.1103/PhysRevD.33.3495). URL: <https://link.aps.org/doi/10.1103/PhysRevD.33.3495>.
- [37] Carlos H Faham. "Prototype, Surface Commissioning and Photomultiplier Tube Characterization for the Large Underground Xenon (LUX) Direct Dark Matter Search Experiment". In: (2014). DOI: [10.7301/Z0QV3JV5](https://doi.org/10.7301/Z0QV3JV5). URL: <https://repository.library.brown.edu/studio/item/bdr:386139/>.
- [38] Carl Eric Dahl. "The physics of background discrimination in liquid xenon, and first results from Xenon10 in the hunt for WIMP dark matter". PhD thesis. Princeton U., 2009.
- [39] J Lindhard et al. "INTEGRAL EQUATIONS GOVERNING RADIATION EFFECTS. (NOTES ON ATOMIC COLLISIONS, III)". In: *Kgl. Danske Videnskab., Selskab. Mat. Fys. Medd.* 1 (Jan. 1963). URL: <https://www.osti.gov/biblio/4701226>.
- [40] Peter Sorensen and Carl Eric Dahl. "Nuclear recoil energy scale in liquid xenon with application to the direct detection of dark matter". In: *Physical Review D* 83.6 (Mar. 2011). ISSN: 1550-2368. DOI: [10.1103/physrevd.83.063501](https://doi.org/10.1103/physrevd.83.063501). URL: <http://dx.doi.org/10.1103/PhysRevD.83.063501>.
- [41] G.J. Alner et al. "First limits on WIMP nuclear recoil signals in ZEPLIN-II: A two-phase xenon detector for dark matter detection". In: *Astroparticle Physics* 28.3 (Nov. 2007), pp. 287–302. ISSN: 0927-6505. DOI: [10.1016/j.astropartphys.2007.06.002](https://doi.org/10.1016/j.astropartphys.2007.06.002). URL: <http://dx.doi.org/10.1016/j.astropartphys.2007.06.002>.
- [42] G Heusser. "Low-Radioactivity Background Techniques". In: *Annual Review of Nuclear and Particle Science* 45.1 (1995), pp. 543–590. DOI: [10.1146/annurev.ns.45.120195.002551](https://doi.org/10.1146/annurev.ns.45.120195.002551). eprint: <https://doi.org/10.1146/annurev.ns.45.120195.002551>. URL: <https://doi.org/10.1146/annurev.ns.45.120195.002551>.
- [43] E. Aprile et al. "Intrinsic backgrounds from Rn and Kr in the XENON100 experiment". In: *The European Physical Journal C* 78.2 (Feb. 2018). ISSN: 1434-6052. DOI: [10.1140/epjc/s10052-018-5565-y](https://doi.org/10.1140/epjc/s10052-018-5565-y). URL: <http://dx.doi.org/10.1140/epjc/s10052-018-5565-y>.
- [44] D.S. Akerib et al. "Radiogenic and muon-induced backgrounds in the LUX dark matter detector". In: *Astroparticle Physics* 62 (Mar. 2015), pp. 33–46. ISSN: 0927-6505. DOI: [10.1016/j.astropartphys.2014.07.009](https://doi.org/10.1016/j.astropartphys.2014.07.009). URL: <http://dx.doi.org/10.1016/j.astropartphys.2014.07.009>.
- [45] S. Agostinelli et al. "Geant4—a simulation toolkit". In: *Nuclear Instruments and Methods in Physics Research Section A: Accelerators, Spectrometers, Detectors and Associated Equipment* 506.3 (2003), pp. 250–303. ISSN: 0168-9002. DOI: [https://doi.org/10.1016/S0168-9002\(03\)01368-8](https://doi.org/10.1016/S0168-9002(03)01368-8). URL: <https://www.sciencedirect.com/science/article/pii/S0168900203013688>.

- [46] D.S. Akerib et al. "LUXSim: A component-centric approach to low-background simulations". In: *Nuclear Instruments and Methods in Physics Research Section A: Accelerators, Spectrometers, Detectors and Associated Equipment* 675 (2012), pp. 63–77. ISSN: 0168-9002. DOI: <https://doi.org/10.1016/j.nima.2012.02.010>. URL: <https://www.sciencedirect.com/science/article/pii/S0168900212001532>.
- [47] J. B. Albert et al. "Measurement of the drift velocity and transverse diffusion of electrons in liquid xenon with the EXO-200 detector". In: *Physical Review C* 95.2 (Feb. 2017). ISSN: 2469-9993. DOI: [10.1103/physrevc.95.025502](https://doi.org/10.1103/physrevc.95.025502). URL: <http://dx.doi.org/10.1103/PhysRevC.95.025502>.